Photonic Flat Bands in Dielectric Metasurfaces

Christopher Woods Munley

A dissertation submitted in partial fulfillment of the requirements for the degree of

Doctor of Philosophy

University of Washington

2023

Reading Committee:

Arka Majumdar, Chair

Xiaodong Xu

Miguel Morales

Program Authorized to Offer Degree

Physics

University of Washington

Abstract

Photonic Flat Bands in Dielectric Metasurfaces

Christopher Woods Munley

Chair of the Supervisory Committee:

Arka Majumdar

Department of Physics

Abstract: Photonic flat bands allow for the realization of angle-insensitive, wavelength-selective resonances. By engineering the meta-atoms of a dielectric metasurface, a photonic band can be realized that is flat along one principal axis of momentum, and by additionally engineering the symmetry of the lattice, a locally flat photonic band can be realized in all directions around the gamma point of the Brillouin zone. Measurement of these devices with energy-momentum spectroscopy can be used to confirm their flat band dispersion. The one-dimensional flat band metasurface is used to demonstrate dispersion engineering of visible emitters. Potential applications for one- and two- dimensional photonic flat band metasurfaces are discussed.

Table of Contents

Dedication

To My Family: Past, Present, and Future

List of Figures

5.3 Demonstration of the fitting procedure and robust loess filter smoothing. The simulated flat band E-k spectrum is shown in black and white with fitted resonances plotted as red dots. The dashed red line represents the band structure fitting with a robust loess smoothing filter applied to the Fano resonant wavelengths. Note that the band itself is not the dip or peak of transmission or reflection but instead exists in between at the resonant wavelengths. Outside the primary fitting region, the extracted wavelengths of Fano resonances are spurious and excluded from the smoothing filter (red dots at edges of image).

6.1 (Adapted with permission from C. Munley ACS Photonics) a) Design dimensions of the unit cell of the one-dimensional flat band, showing the parameters, a, the period, FF, the fill factor, α, the period-doubling asymmetry, the height, h, and the partial etch depth h_1. Note that the measured angle of the flat band, θ, is along the length of the bars. b) Simulated flat band dispersion from the designed metasurface

6.2 Illustration of the steps of fabrication for the suspended GaP membrane structure. Resist is deposited and subsequently patterned via electron beam lithography. After calibration of the etch rate, a directional etch is applied to partially etch the GaP membrane in order to create vertical-symmetry-breaking in the structure. After the directional etch and dissolution of the first resist mask, a second round of resist, patterning and directional etch is performed to open trenches down to the silicon substrate around the metasurface. In between these trenches, patches of unetched GaP are left to support the soon-to-be-floating metasurface. Finally, a silicon-selective isotropic etch is used to dissolve the underlying silicon substrate, leaving the metasurface floating.

6.3 (Adapted with permission from C. Munley ACS Photonics). Visible and electron microscopy images showing the array of device, the flat band device, and a scanning electron microscope image of the details of the device. From left to right, scale bars are 50um, 10um, and 1um.

7.1 Image of the fabricated chip showing floating GaP membrane metasurfaces with a fabricated array varying in period and fill factor to account for fabrication error.

7.2 (Adapted with permission from C. Munley ACS Photonics) Simulated (top) vs measured (bottom) E-K spectra with extracted photonic band fits (red dashed line) showing the evolution from a flat band to a multivalley band.

7.3 (Adapted with permission from C. Munley ACS Photonics SI) a), b), c) TEM images of a representative CdSe nanoplatelet suspension with callout of measured six monolayer thickness. Note homogeneity of NPL thickness and inhomogeneity in lateral dimensions. d), e) Histogram of the measured lateral dimensions of the NPL. f) Measured photoluminescence spectrum of a CdSe NPL sample without flat band device. Main peak with full-width at half-max shown as 10.1nm and note a much smaller peak that derives from the impurity species of seven monolayer-thick CdSe NPL.

7.4 (Adapted with permission from C. Munley ACS Photonics SI): Full energy-momentum spectroscopy of the photoluminescence of CdSe nanoplatelets on the GaP flat band metasurface (top) along with an integration of the red-highlighted portion to produce a one-dimensional spectrum showing enhancement of emission at the flat band wavelength (bottom).

8.1 Verification that the one-dimensional photonic flat band is not accidentally a two-dimensional photonic flat band! Dispersion along y-axis with P-polarized light (left) is locally flat near the Γ point with the fit flat band shown (red-dashed line), while dispersion along the x-axis with P-polarized light (right) shows significant dispersion in the vicinity of the Γ point.

8.2 Photonic band structure evolution from the one-dimensional flat band structure to a two-dimensional lattice of square resonators, shown as a function of the vertical scaling factor applied to the height of the one-dimensional bar elements.

8.3 Band structure of a square-element Lieb lattice optimized for flat bands along the X axis of the band structure in both polarizations. However, note the extremely dispersive bands along the M axis, indicating these flat bands do not extend across momentum space in two dimensions.

8.4 Scanning electron microscopy images of the suspended GaP Lieb metasurface based on a lattice of square posts. Top-down view (left) showing a large number of small elements, and an oblique view (right) where the beginning of buckling can be seen in the gallium phosphide membrane. Beneath the floating membrane the rough surface of the undercut silicon can be seen.

8.5 Experimentally measured photonic band structure along the X axis of the Brillouin zone with S polarization as a function of fill factor across multiple devices. Starting from lowest fill factor (C3R5), the devices transition to nominal fill factor (R5C5), and finally to highest measured fill factor (C7R5). Color bars showing counts (arbitrary units) are displayed next to each measured band structure. The resolution of the bands is quite low, most likely due to fabrication disorder.

8.6 Comparison of band structure as a function of eccentricity of the linking lattice elements showing X and M momenta axes and S and P polarization axes. While the flat band in the Lieb lattice (left) touches other bands, the band is shifted away from its neighbors as the eccentricity increases to the fabricated "standard" (center). As the eccentricity further increases the band dispersion itself changes, shifting to a multivalley dispersion (right). Note that as the eccentricity of these elements increases, the band in question also narrows showing an increase in the quality factor of its resonance.

8.7 Field profiles and intensities for various incoming polarizations at the top of the metasurface at the air-silicon interface. Here, $E\text{-}P^2$ is the intensity due to P-polarized input light with field components $E\text{-}P_x$, $E\text{-}P_y$, and $E\text{-}P_z$. Similarly, $E\text{-}S^2$ is the intensity for S-polarized input light with field components $E\text{-}S_x$, $E\text{-}S_y$, and $E\text{-}S_z$.

8.8 Field profiles and intensities for various incoming polarizations in the middle of the partially etched silicon metasurface. Here, $E\text{-}P^2$ is the intensity due to P-polarized input light with field components $E\text{-}P_x$, $E\text{-}P_y$, and $E\text{-}P_z$. Similarly, $E\text{-}S^2$ is the intensity for S-polarized input light with field components $E\text{-}S_x$, $E\text{-}S_y$, and $E\text{-}S_z$.

8.9 Field profiles and intensities for various incoming polarizations at the bottom of the metasurface at the silicon-quartz interface. Here, $E\text{-}P^2$ is the intensity due to P-polarized input light with field components $E\text{-}P_x$, $E\text{-}P_y$, and $E\text{-}P_z$. Similarly, $E\text{-}S^2$ is the intensity for S-polarized input light with field components $E\text{-}S_x$, $E\text{-}S_y$, and $E\text{-}S_z$.

8.10 Study of etch dependence of two-dimensional flat band structure showing X and M momenta axes and S and P polarization axes. The band structure of the intended "standard" partial etch depth is shown (center), along with variation in the partial etch depth showing under-etching (left) and over-etching (right). Note correlated transition from multivalley dispersion to parabola as the partial etch depth changes.

8.11 Study of the photonic flat band's dependence on fill factor. Spectra here are shown in transmission.

8.12 Simulated band structure of the flat band metasurface along 15-degree rotational steps in azimuthal angle from along the X axis is in the Brillouin zone ($\phi = 0°$) to along the M axis ($\phi = 45°$) for both S and P polarizations.

9.1 Experimentally measured band structure of the flat band metasurface along 15-degree rotational steps in azimuthal angle from along the X axis is in the Brillouin zone ($\phi = 0°$) to along the M axis ($\phi = 45°$) for both S and P polarizations.

9.2 Comparison of simulated band structure with experimentally measured band structure for the Lieb lattice metasurface. Note a wavelength offset of 10nm between the simulation and experiment, which is most likely due to fabrication imperfections.

9.3 Comparison of simulated band structures with (bottom) and without (top) loss in the silicon. The top row of RCWA simulations assumes a defined refractive index of 3.67 for the silicon while the bottom row uses the Lumerical 'Silicon- Palik' material which includes an imaginary component of the refractive index. The color axis is identical between the two simulation results—note a significant decrease in the amplitude of the Fano resonance for the simulation including loss.

9.4 Extracted band structures shown for both S and P polarizations for the theoretically simulated and experimentally observed results.

9.5 Limits of the flat band indicated on the two-dimensional band structure with corresponding unit cell field intensities shown. Note isolation of the field to the sublattices when excited along the principal axes of symmetry.

9.6 Reflection spectra of the flat band metasurface taken with a 10x objective up to a numerical aperture of .25. Note the extent of the flat bands out to ~8 degrees of half angle. Bound states in the continuum can also be observed with specific selection symmetries at ~730nm and ~750nm.

10.1 Simulated band structure of the 2-D flat band metasurface with a material having a refractive index of 1.5 added to one of the elliptical elements (for example, Poly(methyl methacrylate)). This breaks the degeneracy between the flat bands associated with field confinement in each of the elliptical elements (while also perturbing them out of a flat dispersion). This illustrates the ability of a refractive index change in only one of the elliptical elements to selectively shift bands of a specific polarization and incident angle. The band structure is now shown along the X, M, Y, and M' axes of the Brillouin zone with the M' axis at an azimuthal angle, $\phi = 135°$.

Foreword and Acknowledgement

Although I am new to the world of research (and by extension, academia), I am eager to study its patterns just as I am to study the patterns of nature. In my graduate work, I have noticed that research seems to return cyclically to themes over and again, and that in doing so, we in turn complicate and simplify the subject at hand. And so it is with photonics. At the beginning of my Ph.D. I was quite afraid of "doing something that had been done before," but near its conclusion it is comforting to accept that science is an iterative endeavor and hope that my work will affect future researchers just as past researchers have guided me. The study of non-dispersive behavior in photonics has its origins in the past with studies of slow light in waveguides and photonic crystals, but with new technology and even new fields of study, we can return to these concepts and hopefully offer something new.

I would like to thank all of the physics teachers and supervisors who have inspired and mentored me throughout the years, including Dr. John Makous, Dr. Kater Murch, Dr. Kai-Mei Fu, Dr. Josh Hendrickson, and especially Dr. Arka Majumdar. Thank you as well to my Ph.D supervisory committee including Brandi Cossairt, Miguel Morales, Mark Rudner, and Xiaodong Xu. I also tremendously appreciate my first non-physics supervisor, Glenn House, for allowing me to experience the world outside of physics research, and for showing me effective team management and mentorship. I view research as a team endeavor, and it is truly the support of my labmates that taught me the most in graduate school and helped me to succeed in research. To everyone that has sat down and had an insightful (or somewhat silly!) discussion with me about physics, research, or life, I extend my heartfelt gratitude. I would like to thank all members of the Majumdar lab, especially my co-authors David, Arnab, Johannes, Minho, Jie, Elyas, Rui, Roger, Hannah, Abhinav, Quentin, and Forrest. My time at AFRL was especially helpful

in helping me decide what I want to do after graduate school, and I especially thank Josh and Chris for being amazing co-workers and mentors. My friends in Seattle, especially Josh, Jared, Alex, and Jared, were instrumental to my success, and I wish them all the best in their own endeavors!

My most important support, of course, comes from my family. My parents have supported my interest in science my entire life, up to and especially including graduate school, and I am forever grateful for their love and support. Thank you to my brother, Jack for always taking an interest in my research and supporting me no matter what. Finally, my unending love to my fiancée, Lorryn. It is her support and inspiration that helped me when times were tough, and I look forward to our future together. Thank you for all of your support throughout my Ph.D. I give thanks to God for all the opportunities I have and the sustainment to face them. And of course, thanks to my wonderful cat, Frankie.

1. Introduction

While photonic crystals have been studied for quite some time, it is only more recently that the field of optical metasurfaces has been widely researched [1,2]. These optical metasurfaces (here termed metaoptics) have since demonstrated many of the capabilities of traditional optics and even surpassed them by offering control over parameters that traditional optics cannot hope to match [3]. From their advent, metaoptics have offered remarkable imaging performance which has only improved with the even-more-modern application of software image processing [4]. However, as we look beyond the prospect of imaging, there are many additional degrees of freedom where metaoptics may offer control. In particular, spectral and angular control of light have become intriguing use cases for the customization that metaoptics offer. It is at this intersection of metaoptics, spectra, angular control, and photonic crystal band structure that we find the concept of a photonic band with flat dispersion, hereafter termed a photonic flat band.

Herein, I will describe some of the background knowledge required to study photonic flat bands and dielectric metasurfaces before discussing the creation of one-dimensional (1-D) and two-dimensional (2-D) visible and near-infrared flat bands in dielectric metasurfaces. I will also outline the numerical simulations used to design these metasurfaces and the experimental setups used to measure them, as well as the nuances of comparing simulated and experimental results. The 1-D metasurface displaying flat band dispersion is used as a platform to demonstrate dispersion engineering of colloidal emitters in the visible regime. Finally, I present some thoughts about current and future applications of photonic flat band metasurfaces including collaborative work on photonic flat bands used in a narrowband angle-insensitive photodetector and several potential use cases for the two-dimensional flat band metasurface. It is my hope that this work will

not only comprehensively summarize what I have learned investigating photonic flat bands in dielectric metasurfaces but will also highlight the many opportunities for these frameworks and techniques to be applied to novel metaoptics in the future.

1.1 Breakdown of Chapters

Chapter 1: Introduction

Chapter 2: Background

Here I will outline the history of metaoptics and the history of photonic flat bands before overviewing the current state of the art in creating photonic flat bands.

Chapter 3: Simulating Photonic Band Structure

This chapter covers the history and fundamentals of rigorous coupled wave, which is used for the simulations of photonic band structure. It also highlights specific notes on the parameters used for the presented band structures.

Chapter 4: Energy-Momentum Spectroscopy

Here I go through a variety of methods to measure the band structure of photonic metasurfaces before focusing specifically on the energy-momentum system used for experimental measurement of the flat band metasurfaces in this dissertation. The optical components used in this system are described and a procedure for alignment is listed.

Chapter 5: Comparing Simulation and Experiment

This chapter works through the process of fitting the characteristic Fano resonances measured in photonic band structure measurements. Furthermore, I work through the background fitting process and extraction and fitting of the photonic bands in one and two dimensions.

Chapter 6: 1-D Flat Band Design

The one-dimensional flat band design is derived from literature and transitioned to the visible regime in a gallium phosphide platform. This chapter also discusses the nuances of fabricating the flat band metasurface and designing a chip robust to fabrication tolerances.

Chapter 7: 1-D Flat Band Results

The experimentally measured photonic band structure of the one-dimensional flat band metasurface is presented along with measurements of various other photonic band structures present on the same chip. Cadmium selenide nanoplatelets are then integrated with the chip and the dispersion of the coupled flat band photoluminescence is measured.

Chapter 8: 2-D Flat Band Design

This chapter works through the design process of the two-dimensional flat band, first as a transition from the one-dimensional flat band design in the visible regime and then starting from a Lieb lattice in silicon for a near-infrared flat band. Again, mitigating strategies for fabrication errors are discussed with respect to the two-dimensional flat band metasurface chip.

Chapter 9: 2-D Flat Band Results

Measurements at two different numerical apertures from the two-dimensional flat band metasurface are presented and discussed. Correspondence between the band structure and the simulated field intensities of metasurface is discussed.

Chapter 10: Applications

Here, various applications of photonic flat bands are discussed ranging from uses in astrophotonics to narrowband filtering in trapped ion quantum computing. Work on

integration of a one-dimensional flat band with a photodetector is discussed, along with a focus on the angle-insensitive filtering applications for a two-dimensional flat band. Finally, more speculative applications are discussed.

Chapter 11: Conclusion

2. Background

While optics is one of the oldest fields of science, the study of sub-wavelength diffractive optics metaoptics is one of its newest [5]. The creation of new tools to pattern metal and dielectric materials at the subwavelength scale has led to the advent of metaoptics. Throughout the history of optics, efforts to decrease the size of individual lenses have led to the technological progression of traditional refractive lenses to Fresnel lenses, Fresnel zone plates, multilevel and binary diffractive lenses, and finally to metalenses. Each shift in theory and design changes the overall size of the optical elements, but also allows for the emergence of new opportunities along with new challenges for optical systems. In this chapter, I will walk through the development of meta-optics, the development of photonic flat bands, and current platforms that have been used to study optical flat bands.

2.1 Fresnel Optics

The Fresnel lens is often introduced as the first step in the development of metaoptics because it begins the progression to thinner and thinner optics. A Fresnel lens' behavior can be understood by imagining a traditional lens and implementing a wrapping condition on the thickness of the lens. As refractive lensing depends on the angle of the surface of the lens, the thickness can be reduced while maintaining the same optical effect. Thus, the thickness of the lens can be limited while only introducing sparse one-dimensional discontinuities in the angle and thickness of the lens. In this system the discontinuities are mostly ignored, and the behavior of the continuous parts of the lens are explained in terms of traditional ray optics.

However, the benefits of phase engineering were not lost on early optical pioneers. On the other side of the same coin, Fresnel zone plates use discontinuities as diffractive elements to create an image. While initially simple, zone plates eventually developed

into multilevel zone plates and more recently into photon sieves, which incorporate broken azimuthal symmetry to bring diffractive optics closer to the focal limit [6]. The advent of sub-wavelength patterning techniques allowed for the invention of metalenses, bringing diffractive optics to its inevitable conclusion—an optical surface composed almost entirely of discontinuities. By introducing sub-wavelength phase discontinuities at essentially every point on a surface, what was previously accomplished with refraction is done entirely with diffraction.

2.2 Metaoptics

While diffraction limited performance of metaoptics seeking to reproduce traditional lenses (hence, metalenses) was reported from the outset, eliminating chromatic aberration in imaging remains an open issue [2]. Despite obstacles in improving upon classical imaging, the ability to fabricate arbitrary sub-wavelength elements (often called meta-atoms) has led to a renaissance in optical engineering even beyond phase engineering with research on controlling the wavelength, polarization, angle, and quantum properties of light all using metasurfaces [7]. Functionally, the focus beyond phase control has significantly broadened the field of metaoptics and developed connections between the concepts of optical metasurfaces, photonic crystals, high contrast gratings, and even traditional freeform optics. There is perhaps some controversy over advantages of metaoptics and what deserves to be given the title "metaoptic" or "metasurface" [8,9]. Given its "meta" nature, I believe it is appropriate to define any surface of elements designed for out-of-plane excitation to be a metaoptic. While some may argue that such a broad definition is diluting to the focus of the field, on the contrary, I believe that by incorporating the design strategies of as many devices as possible we open new avenues for creative design.

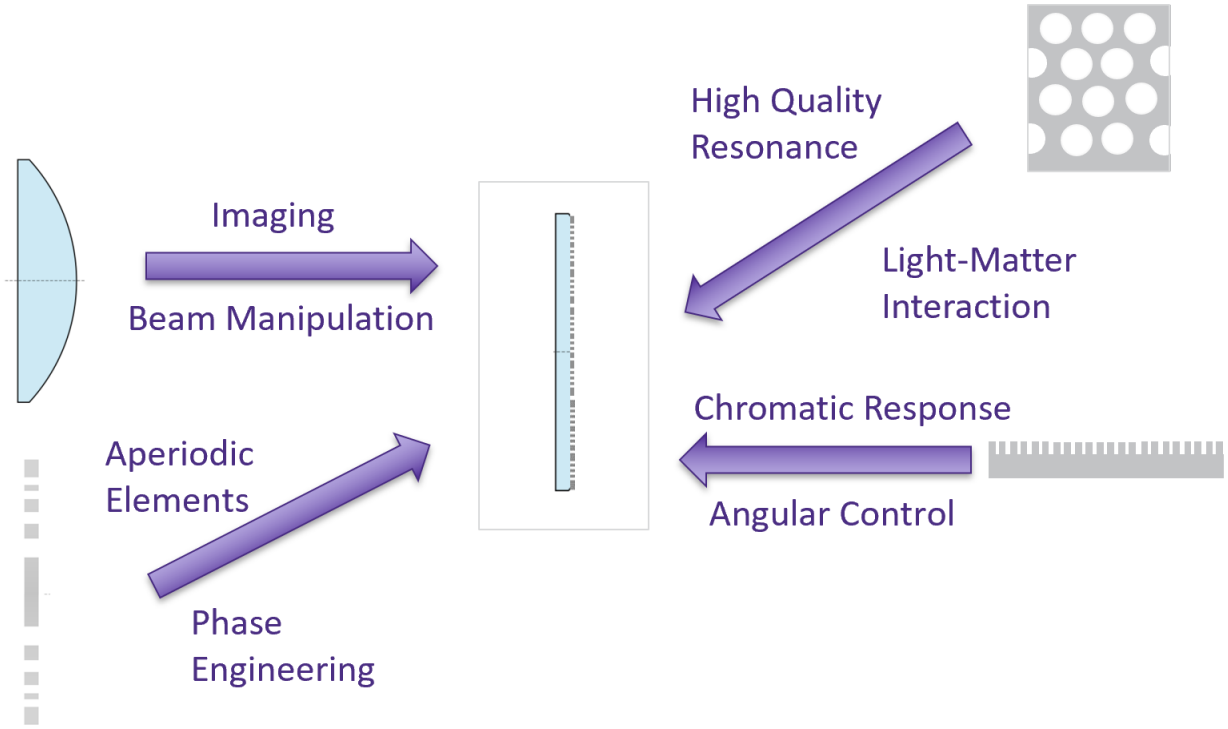

Figure 2.1: Inspiration for metaoptics can come from many different types of devices, including (represented clockwise from top) photonic crystals, diffraction gratings, photon sieves, and lenses. Each discipline contributes new concepts and goals to metaoptics design.

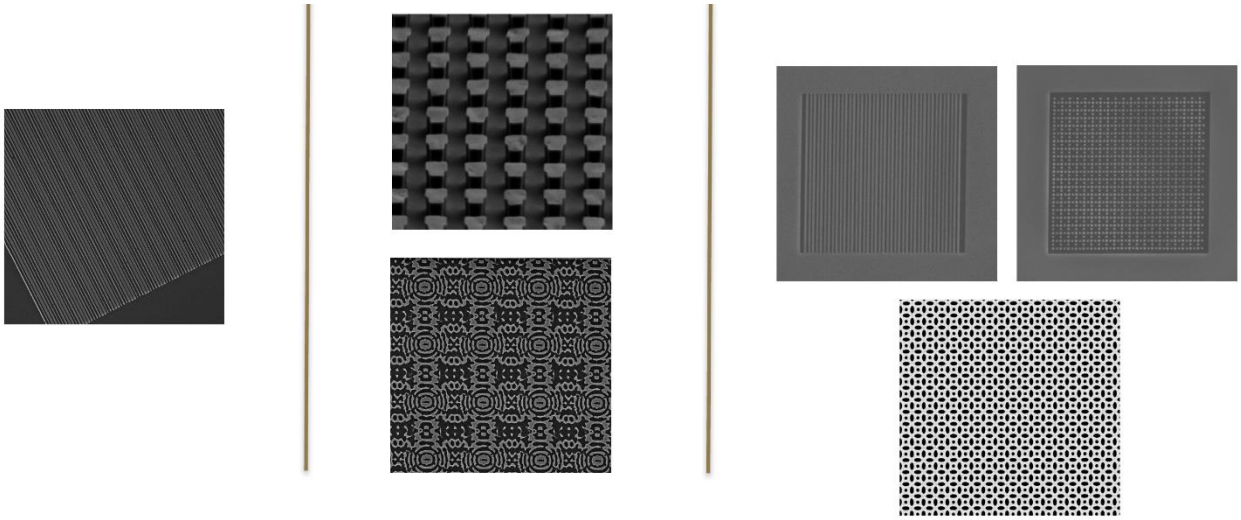

Figure 2.2: The diversity of metasurfaces as shown by a variety of different metasurfaces grouped by function. From left to right: a metalens that combines focusing with color filtering to mimic the human eye, two metasurfaces for enhancing light-matter interaction via a bound state in the continuum and inverse design, and three metasurfaces engineered to demonstrate flat band dispersion.

Recently, angular and spectral control of light in metaoptics have been categorized as "nonlocal metaoptics" (objections of physicists, notwithstanding), referring to the fact that control of the momentum of light is a collective property of the elements of the metasurface as opposed to control of the phase of light, which is accomplished on a "local" element-by-element basis [10-12]. These "nonlocal" resonances are a return to earlier studies of photonic crystals and high-contrast gratings, but specifically studied with out of plane excitation and an ability to create arbitrary sub-wavelength patterns. Of course, the collective angular response of a group of elements with a common period can also be viewed as the band structure of the device, and the "nonlocal" angular control accomplished by a metasurface can often be viewed as dispersion engineering of its effective photonic band structure. While there are interesting discussions to be had about almost any band structure, here, we will mainly be focusing on flat photonic bands.

2.3 Photonic Flat Bands

So, what is a photonic flat band? The study of photonic flat bands can be traced back through a variety of naming conventions to the original observation of a slow group velocity of light in a silicon waveguide [13,14]. It was noticed that the dispersion relationship of light in these waveguides could be measured to be even flatter than would be anticipated from the material properties of silicon—evidently the properties of the patterned material were introducing additional "structural" dispersion! The measurement of a slow group velocity of light eventually led to the appreciation that many photonic bands in photonic crystals have very low dispersion at the gamma point of their Brillouin zone, and that this slow group velocity has applications in enhanced nonlinearity and modulation of light in photonic crystals [15]. Beyond the simple observation of "slow light," research also extended into engineering the dispersion of light within photonic-crystal waveguides, going so far as to show controllable transitions between flat dispersion and multi-valley dispersion [16]. However, the paradigm of these

investigations was to consider integrated photonics as analogous to integrated circuits, and rarely considered coupling to free space as anything but a loss channel—after all, it is extraordinarily rare to find electrons transiting outside the plane of electronic circuits and in most cases extremely undesirable!

The concept of a photonic flat band is inextricably linked to measurements of dispersion and band theory. However, the main measured phenomenon of a photonic flat band in a metasurface is an angle-insensitive optical response. What distinctions can be made to conclusively identify a photonic flat band? If an angle-insensitive optical response is all that is required, many bulk materials satisfy this requirement! As a random collection of oscillators will lack any preferred direction, the optical response of disordered media is angle insensitive. It is exactly this type of material that is used for traditional color filtering with absorptive films, however the wavelength-selectivity of these filters is fundamentally limited by the bandwidth of their absorptive material. It is also possible to demonstrate angle-insensitive filtering with structural resonators that remain uncoupled, but to my knowledge this is traditionally done with plasmonics and does not provide a platform for band structure engineering. A true flat band of coupled resonators creates an extended and coupled mode which has the same resonant energy over a range of in plane momenta or incident angles. The wavelength-selectivity of this mode, which is reinforced by its periodic nature, can be very high and represents a platform to build upon with other band engineering techniques.

It is also possible to realize photonic flat bands as a property of an extended array of resonators that is not necessarily periodic or has a very large unit cell. This has been shown through the use of fractal geometries such as the Sierpinski lattice [17, 18]. This may be useful for certain applications, but in studying flat bands specifically in photonic metasurfaces, our goal is to obtain a homogenous, material-like response from the metasurface. A homogenous response would be especially useful for filtering or

applications in photodetection, because otherwise light focused onto one point of the extended array may experience a different response than light focused on another point.

As modern fabrication and measurement methods have come into use, attention has returned to the subject of structurally engineering a low dispersion of light under the title of "photonic flat bands" [19]. A variety of different systems have been used to realize photonic flat bands, but perhaps the leading system for experimenting with dispersion engineering and novel photonic band structure is arrays of coupled waveguides. Flat band dispersion in a lattice was shown in a laser-written array of waveguides, and laser-written arrays of waveguides remain a popular model system to study photonic flat bands [20, 21]. In these systems, input and output states can be easily controlled by selectively exciting and measuring specific waveguides within the lattice. This ease of control and measurement, along with the three-dimensional configurability of laser-written waveguides is what makes this system attractive to study even today [22]. Laser-patterned arrays of waveguides are important for theoretical studies and for studying applications in photonic crystal fibers and analogous systems but remain bulky and impractical for free-space-coupled applications.

2.4 Photonic Flat Bands in Various Systems

Arrays of resonators, sometimes coupled with actively emitting material have been used to demonstrate photonic flat bands [23] and can be coupled with free-space light. Site-selective control and integration of active materials make this an exciting platform for manipulating polariton dynamics, but this is a significantly different pursuit than the production of a metamaterial, in which a given device which can display new material properties as opposed to site-selective phenomena. There have been significant previous studies of photonic flat bands in metaoptics. Hai Son Nguyen has notably contributed to the field of photonic flat bands with work on perovskite metasurface flat

bands, slow light in photonic metasurfaces, and Moiré flat bands [24-26]. Of most immediate import, they experimentally demonstrated one-dimensional photonic flat bands in the infrared regime and theoretically explained their appearance and tunability [27]. This paper was the beginning of my interest in photonic flat bands and remains an important experimental demonstration of photonic flat bands in metaoptics. However, many of the studies on photonic flat bands in metaoptics remain theoretical and their designs impractical for fabrication, illuminating the gap between flat band theorists and the experimental metaoptics community.

Flat bands have been realized in plasmonic systems by tailoring both individual elements and lattice symmetries. A lattice constructed of self-similar meta-atoms was observed to have a flat band response [28]. And construction of a Lieb lattice metasurface for terahertz spoof plasmons was shown to have flat band dispersion, as well [29]. These terahertz responses are in a completely different regime than the study of photonic flat bands in the visible and near-IR, but they do offer some inspiration in avenues of study.

There has been some beginning interest in the applications of photonic flat bands with studies on coupled waveguides showing the usage of flat band to preserve image transmission in a Lieb lattice [30]. Material integration with flat bands has been explored to demonstrate exciton-polariton lasing, and dispersion engineering has been studied to generally reduce the threshold for lasing in coupled waveguide structures [31,32]. In an interesting turn of events, photonic flat bands have also been shown to enhance the emission of free-electron radiation, which may find photonic flat bands applications in particle accelerators [33].

More recently, with increasing interest from the condensed matter community focusing on Moiré physics, the concept of Moiré flat bands has been realized in photonic crystal metasurfaces. Two-dimensional material systems exhibiting Moiré lattices based on graphene, hexagonal boron nitride, and transition metal dichalcogenides (TMDCs)

rely on layering homo- or hetero-bilayers to produce Moiré patterns. While this approach has been theorized in photonics, it is also possible to create a Moiré pattern by merging what would typically be two layers of material into a single layer containing a "merged" Moiré pattern. This structure has recently been used to show a site-selective lasing array and may find further uses as an evolution of the concept of the photonic crystal surface-emitting laser [34, 35].

3. Simulating Photonic Band Structure

While the photonic band structure of a given lattice can be calculated numerically under certain assumptions, in order to best compare with the measured reflectance of the device as a function of wavelength and incident angle, rigorous-coupled wave analysis (RCWA) can be used to simulate this response in a numerical manner. Here we will discuss the history of RCWA and some technical notes on the parameters used for simulation of photonic flat bands.

3.1 Rigorous Coupled Wave Analysis (RCWA)

Originally formalized by M. G. Moharam and T.K. Gaylord, RCWA was improved upon over the years and eventually integrated in a package developed by Victor Liu and Shanhui Fan, known as the Stanford Stratified Structure Solver, or S^4 [36-39] RCWA is formulated specifically for analysis of the optical response of layered materials to light with different incident angles, polarizations, and wavelengths—in short it is the perfect match for the experimental analysis of the photonic band structure of metasurfaces! Subsequently, the commercial product, Lumerical, has integrated an extremely similar RCWA solver seemingly based on S^4 which allows for interoperability between RCWA and finite-difference-time-domain (FDTD) analysis. Most simulated results presented here were simulated within this environment.

The standard layout of an RCWA analysis is to define a number of layers of material with specified index of refraction (real and imaginary), and then apply lateral patterns to these layers (either holes, or extended elements). Next, a definition for the incoming light is provided and the ranges of wavelengths and angles to sweep are specified. A simulation of the response of the layered structure to a plane wave for each of these wavelengths and angles is performed with each of these simulations recording local fields along with the coefficients of transmission and reflection. Final analysis can

then be performed on the recorded data. There is no real consideration of time-dependent effect, to my knowledge, and this is one of the major drawbacks of RCWA as opposed to an FDTD solver. However, the speed and utility of RCWA prevail and I find it the most effective way to calculate photonic band structures for devices that are intended to be illuminated with non-pulsed light.

It is perhaps typical to simulate with RCWA as a function of energy and incident angle, and this is certainly useful when doing exploratory simulations to build intuition, but in order to eventually compare results with experiment, it is desirable that the final RCWA results be a function of the wavelength and sine of the incidence angle of incoming light. Of course, one can be transformed into the other, but to maintain constant pixel size across an image, it is best to simply use the wavelength and sine of the incident angle as the sweeping parameters within the RCWA simulation when producing final results. In this way if the wavelength range captured by the spectrometer is input to the simulation as the range of wavelengths and the numerical aperture of the microscope is input as the maximum sine of the incident angle, the resulting RCWA results for the reflection or transmission coefficients will directly represent what should be obtained when measuring the sample in reflection or transmission.

3.2 Technical Notes

The simulations presented herein consist of single unit cells with 50 or 100 k-vectors comprising the max number of momentum vectors simulated. The simulated field intensities are calculated at 200 simulated k-vectors to provide better resolution. Circular and elliptical elements were simulated as 100-point polygon approximations. The refractive indices of the gallium phosphide, crystalline silicon, and quartz used are set to be 3.37, 3.67, and 1.76, respectively, based on thin film measurements made near the resonant wavelengths of the devices to be fabricated.

In terms of simulation setup, most importantly, the default simulation injection direction is along the positive z-axis! Especially if a substrate layer is included, the injection direction must be set to 'backwards' to avoid spurious refraction from the substrate layer. There is a two-micron buffer zone included in simulations above and below the device with the substrate continuing to the bottom of the buffer zone. Parameter sweeps of exciting wavelength were simulated at a resolution of .1-1nm, with 1-3 degree steps in incident angle.

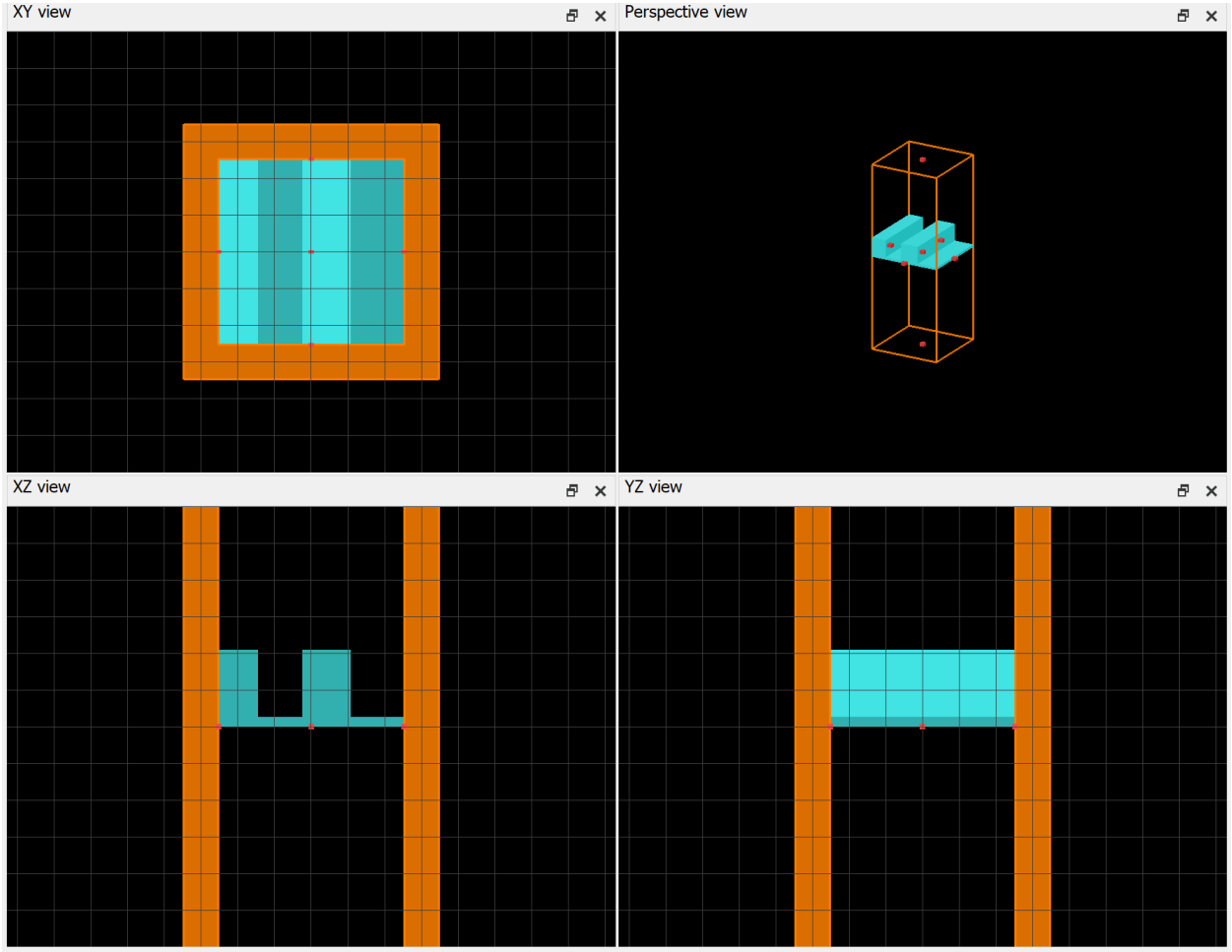

Figure 3.1: Simulation view of the 1-D flat band metasurface showing all views

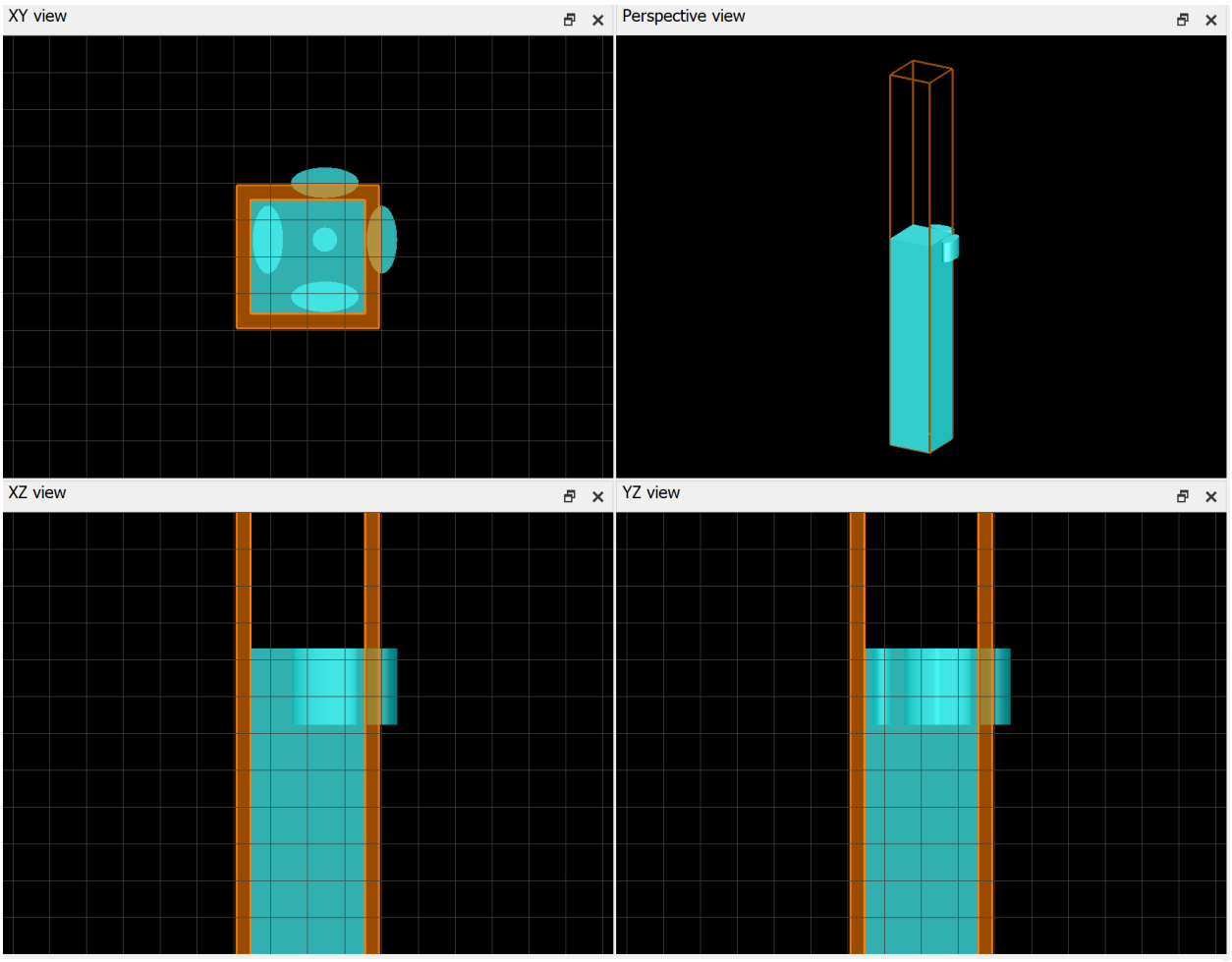

Figure 3.2: Simulation view of the 2-D flat band metasurface showing all views.

4. Energy-Momentum Spectroscopy

To measure the photonic band structure of a device, a measurement setup with sensitivity to wavelength and angle of emission must be used to probe optical response in transmission or reflection. The complete optical band response can be represented as a spectrum at every possible angle of emission or reflection, thus leading to a four-dimensional data structure with two dimensions representing angle of emission, one dimension representing wavelength, and one dimension representing measured optical intensity. This full response is not necessary or practical, however, and by limiting the angular dimension to a given numerical aperture and the measured wavelengths to a region of interest the desired measurement space can be reduced, albeit while remaining four-dimensional. Given this finite but extensive measurement space, the issue at hand becomes measuring and sweeping parameters across this space while maintaining optimal measurement conditions. Walking through various methods of measuring photonic band structure, describing the optics and setup of the specific system used for measuring the photonic flat bands presented here, I hope this section will serve as a comprehensive tutorial on Energy-Momentum (E-k) spectroscopy.

4.1 Methods of Measuring Photonic Band Structure

Several measurement techniques for photonic band response have been developed across the years, each with its own benefits and drawbacks. Most simply, measuring reflection or transmission of a device while manually tilting it allows for the sequential measurement of spectra, but is difficult to control and remains practically a non-starter at cryogenic temperatures. The most common method may be to directly image the Fourier plane of an imaging system while only exciting with one wavelength at a time, but this method cannot accurately determine spectral information from photoluminescence and additionally relies upon anticipating the exact range of a given photonic band structure.

More recently, a technique has been developed to measure by imaging the entire back focal plane of the microscope onto the spectrometer and then deconvolve the spectrometer image and extract underlying spectra and angular information, albeit by relying on several assumptions which makes the setup computational difficult [40]. Toward the goal of versatility of measurement and ease of use, I have instead implemented a form of angle-resolved spectroscopy that we call energy-momentum spectroscopy for its ability to simultaneously image and resolve the spectral and angular information of a given device.

4.2 Energy-Momentum Spectroscopy

Energy-momentum spectroscopy utilizes the two-dimensional nature of a visible spectrometer charge-coupled device camera (CCD) to disperse angular information along the vertical axis of the CCD and spectral information along the traditional horizontal axis, allowing both to be read out for a given polarization and band direction. Using the fact that any standard microscopy system is already measuring along all angles up to the limit of its numerical aperture, the spatial information at the Fourier plane of the microscope (typically the back focal plane of the objective), which represents the angle of incidence to the device, is re-imaged to the input plane of the spectrometer where it is spatially filtered to represent a given axis in momentum space and then diffracted and re-imaged again by the spectrometer to fill out the CCD. In this manner, the light coming off the sample at different angles along a vertical axis is directed to different vertical heights on the spectrometer slit, and then diffracted out to different horizontal positions along the spectrometer CCD. There is then a region on the spectrometer imaging camera that corresponds precisely to the band structure of the device in question, notwithstanding any optical aberrations in the system.

When performed correctly the result is almost magical, as the exact band structure that can be simulated or calculated will appear before your eyes! However, there are untold pitfalls of this method and like the best magic, skilled legerdemain to practice. The main unavoidable drawback of this method is that by dispersing out the signal over a two-dimensional measurement area, it becomes proportionally weaker. For steady-state systems, however, this results only in a longer integration time for measurement and requires a strong broadband input light source. Careful collimation of this input light, sometimes involving the re-imaging of a narrow pinhole, will dramatically improve the quality of the band structure, as well-collimated input light forgives slight misalignment of the output optics. And while the use of a dove prism for image rotation technically allows for measurement of all possible band axes in momentum space, in practice it is easier to just rotate the sample if it is accessible.

Selection of the appropriate optics is necessary not only for the correct spectral range but also for the numerical aperture to be studied, the size of the spectrometer CCD and the distance between the sample and the entrance slit to the spectrometer. While I have often idly dreamed of somehow directly mounting a spectrometer right on top of a cryostat so that the entrance slit is somehow at the back focal plane of the in-cryo objective, this is impossible for many reasons (not the least of which is that the back focal plane of most modern objectives is located within the housing of the objective itself). Thus, it is necessary to introduce at least one 4-f imaging relay to image the back focal of the objective onto the entrance slit of the spectrometer. Unlike almost every other lab-built optical system this means that for a proper focus, the distance between the back focal plane of the objective and the spectrometer is constrained by the 4-f relay—there is no "infinity space" in the system where a collimated beam can be assumed and directed around the optics table. The total sum of foci encompassed by the 4-f system is determined by the distance between the objective and spectrometer, and the relative

magnification of the 4-f system is determined by the CCD size, spectrometer imaging length, objective back aperture, and objective magnification. Ideally, the 4-f system will utilize, but not completely fill, the spectrometer CCD by imaging the back focal plane (whose dimensions are determined by the objective aperture) with the appropriate total magnification determined by the combination of objective, 4-f system, and spectrometer. It is common to refer to the lens closer to the objective as the Fourier lens.

A rather substantial quirk of this system is that once the distance is fixed, the objective cannot move relative to the spectrometer. This means focusing should be accomplished by movement of the sample relative to the objective, which is fine at room temperature, but may require movement of an entire cryostat if no piezoelectric stages can fit in the cryostat. Another quirk is that when measuring in reflection, the beam splitting element separating the excitation and collection sides of the microscope must be in between the Fourier lens and the objective, often as close to the objective as feasible to allow for a Fourier lens with shorter focal length. Note also that the beam-splitting element should be chosen for identical response for transiting angles up to the numerical aperture to be studied. For this reason, I have often used an appropriate beam-splitting cube over a plate or pellicle optic (which may have significant dispersion relations themselves).

4.3 A Representative E-K System

With all of these constraints, the ideal optical system is fairly constrained, and I will now present a representative E-k system, specifically outlining the optical components.

In this representative E-k system a single 4-f system is used to image the back focal plane of the objective onto the input slit of the spectrometer. The source (white light or

laser light) is coupled in through a beam splitting cube located in between the Fourier lens and the objective, as previously discussed.

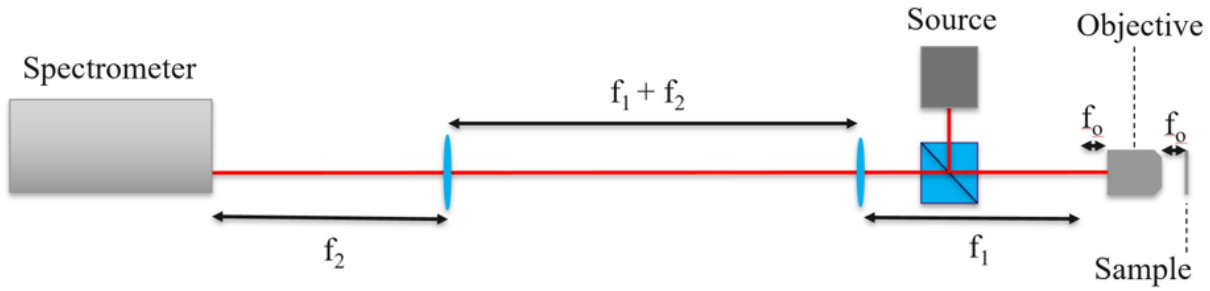

Figure 4.1 (Adapted with permission from C. Munley ACS Photonics). A representative energy-momentum (E-k) spectroscopy system with one 4-f system imaging the back focal plane of the objective onto the entrance slit of the spectrometer. The focal lengths of the objective, f_o, the Fourier lens, f_1, and the imaging lens before the spectrometer, f_2, are depicted. Note that the objective is approximated as a single lens with a representative focal length in this image. In actuality, the working distance and position of the back focal plane of the objective determine its positioning.

The system specifications for the E-K spectroscopy setup representative of the work presented here are now outlined. The objective is an Olympus apochromatic 100x objective with a numerical aperture of .95 to provide a large numerical aperture along with low chromatic aberration for white light reflection measurements of the photonic band structure. For measurements at a lower numerical aperture an Olympus 10x objective with a numerical aperture of .25 is used. The working distance of the 100x objective is .35 mm and the back focal plane is located 8mm behind the plane of the objective lens (inside the housing of the objective). The spectrometer is a Teledyne Princeton Instruments Isoplane 320 with an effective focal length of 320mm and an f-number of f/4.6. The spectrometer slit is a manually adjusted bilateral slit with a minimum slit width of .1mm. A minimum slit width is often used for consistency and maximal selectivity across the back focal plane. In order to set the sample sufficiently far from the spectrometer (and incorporate filter, polarizers, and other optics), the focal

lengths of the spectrometer imaging lens and Fourier lens are chosen to be 150mm and 75mm, respectively. This provides approximately 450mm of total optical distance between the spectrometer and the objective along with a 2x angular magnification when imaging the back focal plane onto the entrance slit of the spectrometer. The Fourier lens is a 2-inch-diameter achromat and the spectrometer imaging lens is a 1-inch-diameter achromat.

When measuring E-k spectra in reflection with white light illumination, the other side of the microscope is just as important, however. Appropriately collimated illumination significantly improves the E-k spectroscopy image of the band structure by limiting inhomogeneous sampling and allowing for easier focusing of the illuminating light. First, it is often the case that the device to be measured does not fill the entire field of view of the objective. If the entire field of view is then illuminated and measured, the inhomogeneity in the sample itself will obscure the intended measurement of the photonic band structure of the device. Second, if only a near-diffraction-limited spot is illuminated, the measurement can be taken when the spot is minimized with confidence that the image is mostly in focus. It is to these ends that the illuminating light is collimated out of a single-mode fiber with an achromatic lens (focal length 30mm) and then images a 75 micron pinhole through a lens relay composed of confocal achromatic lenses (60mm and 75mm). This ensures appropriate collimation of the illuminating light and dramatically improves the image quality of the photonic bands.

4.4 Alignment

Unlike traditional microscopy or spectroscopic measurements of photonic integrated circuits, the entire optical path length between the sample and spectrometer is constrained. Because of this, the standard procedures to set up an optical microscopy system must be modified, and I will briefly walk through an explanation of setting up a

sample system. The steps follow from the theoretical design constraints previously discussed, but I found advice from users of other E-k spectroscopy systems to be most helpful when aligning my optics.

An outline of the steps are as follows:

1. Determine the total optical path length of the 4f system used for re-imaging the back focal plane. Selection of these optics is dictated by the numerical aperture intended to be measured and the acceptance aperture of the spectrometer.

2. Determine the vertical level of the spectrometer entrance slit. This will be the beam height for the entire optical system, including the objective and sample.

3. Lay out the spectrometer imaging lens and the Fourier lens in approximately the correct positions and align mirrors so that a beam can be imaged onto the spectrometer CCD with the diffraction grating at its zero order position. These lenses will also be adjusted later for fine-tuning.

4. Affix the objective to a 3-axis stage with x, y, and z micrometers. Use a rigid mount to fix the angle of the objective so that it is strictly parallel to the optical table.

5. Place the beam splitter and objective mount relative to the Fourier lens, giving enough distance for the position of both the Fourier lens and the objective to be adjusted.

6. Mount a reflective blank chip or mirror to the sample stage which should have at least 7 axes of movement, allowing for 3 axes of linear movement (standard micrometers), 3 axes of tilt (optical mount), and 1 axis of rotation around the optical axis of the objective (rotational mount).

7. Remove the objective and use the rigid mounting body to construct a cage system with two apertures in place of the objective.

8. Set up an alignment laser that is well collimated to use for alignment of the system, for example, a simple 532nm green laser or equivalent that is near the center of the studied optical range.

9. Orient the alignment beam so that it passes through the apertures of the objective cage system.

10. Adjust the sample mount so that the beam is retroreflected off of the mirror or blank chip. The sample mount is now normal to the objective mount.

11. Align the retroreflected beam to the spectrometer slit with the Fourier lens and spectrometer imaging lens removed.

12. Adding the spectrometer imaging lens, adjust the position of the lens to focus the beam (at a very low power) to the smallest possible area on the spectrometer CCD.

13. Place a small mirror in between the entrance of the spectrometer and the spectrometer imaging lens. Adding the Fourier lens into the optical path, adjust its focus so that the beam coming off the inserted mirror is collimated.

13. Check the alignment of the spectrometer imaging lens and Fourier lens by removing and adding them to make sure that the focused or defocused beam remains in the same position on the spectrometer CCD. This ensures that the optical axis of the microscope is passing through the center of these lenses.

14. Add the objective back onto the objective mount and focus on the reflective chip or mirror, checking the focus by looking at the back-reflected light from the alignment laser such that the incident and reflected beam are both collimated and of the same beam waist.

15. Double check the alignment of the objective and the lenses by examining the beam on the spectrometer CCD as before to see that it does not change its central

position when removing any of the lenses or while adjusting the focus of the objective.

16. Implement a 4-f imaging system of a pinhole in the pathway of the incoming light. Using the alignment laser to make sure the output beam is collimated, align this beam to the objective so that it is entering the back of the objective normally.

17. Replace the alignment laser with a broadband light source such as a halogen lamp, outcoupled through a fiber.

18. Align the broadband light source to the 4f-system, if needed.

19. Looking at the zero-order reflection of the spectrometer, with the spectrometer slit as open as possible, adjust the position of the objective and sample together to optimize the imaging of the back focal plane of the objective. At the optimal focus, the image should appear uniform across the circular back focal plane with sharp edges that indicate the limits of the back focal plane, in most cases the back aperture of the objective.

20. Replace the mirror or reflective sample with a distributed Bragg reflector (DBR) based Fabry-Perot cavity with a high known quality factor. Realign with the alignment laser to make sure that the DBR cavity is normal to the optical axis.

21. Illuminating with the broadband light source, adjust the position of the objective (while keeping the sample in focus) so that the spectrometer image with the diffraction grating in results in as sharp a line as possible. This is your first E-k spectrum, and the high quality factor and known dispersion of the DBR cavity allow for optimization and diagnosis of the E-k system.

22. With optimized measurement of the DBR cavity, the E-k spectroscopy system is now ready for use!

Through significant experimentation and consultation with other E-k practitioners, this setup and alignment procedure produced the best results when studying the photonic band structure of metasurfaces. Additional components may be added to the system such as a broadband incoherent source for imaging, or various polarizers. However, throughout the process of adding additional elements, the primary optical axis of the E-k system should be respected and if there is any doubt about the alignment, re-checked.

5. Comparing Simulation and Experiment

It is the comparison of simulated and experimentally measured results that can be used to verify the theoretical design behind photonic flat band metaoptics as well as characterize their potential usefulness. Agreement between the simulated and measured band structure verifies the theory behind the design while discrepancies can reveal unforeseen fabrication imperfections or errors in the design and measurement. Minor variation, however, is inevitable, and so it is necessary to use a method of comparison that is tolerant to random error in the measured band structure but sensitive to systemic error potential caused by faulty theoretical assumptions. Maintaining parity between simulation and experiment is one way to facilitate comparison and it is in this spirit that energy-momentum spectroscopy and rigorous coupled wave analysis are both used to generate reflection data as a function of input angle and wavelength so that they may be directly compared. However, the photonic bands themselves offer greater opportunity to compare theory and experiment so that we can determine any shift in the curvature of the photonic bands. While simply looking at the reflection plots will give an observer the impression of the band structure, extraction of specific parameters is necessary for numerical comparison. Thus, I will describe a robust fitting process to extract the photonic bands from the reflection intensity maps generated from RCWA and E-k spectroscopy.

5.1 Fitting Fano Resonances

In these specific metaoptic systems designed to exhibit sharp photonic bands, the intensity modulation of the reflection or transmission is due to interference between the transiting free space light and the bound states of the photonic bands. This manifests as a Fano resonance, characterized by an asymmetric line shape as the two states interfere

and the metaoptic transitions between reflective and transmissive behavior. The characteristic lineshape of a Fano resonance is described by:

$$\sigma = \frac{(\epsilon + q^2)}{\epsilon^2 + 1}, where\ \epsilon = \frac{2(E - E_F)}{\Gamma}$$

Equation 5.1: Lineshape, σ, of a Fano resonance, with energy, E, Fano-resonant energy, E_F, asymmetry factor, q, and linewidth, Γ.

This lineshape can be quite elegantly derived as the addition of a normal Lorentz lineshape and a flat continuum term, along with a mixing term [41]:

$$\sigma = \frac{(q^2 - 1)}{\epsilon^2 + 1}\,(Lorentzian) + \frac{(2q\epsilon)}{\epsilon^2 + 1}\,(Mixing\ Term)\ +\ 1\,(Continuum)$$

$$\epsilon = \frac{2(E - E_F)}{\Gamma}$$

Equation 5.2: Lineshape of a Fano resonance as in Equation .1 but expanded to highlight derivation

This breakdown also illuminates the way in which the terms interact to compose the Fano lineshape. Note that while the sign of the Lorentzian term is determined by the magnitude of q, the "mixing" term is odd with respective to ϵ, the detuning from resonance scaled by the linewidth. It is this "mixing" term that creates the asymmetric lineshape of the Fano resonance, with asymmetry determined by q, the so-called asymmetry parameter. As energy increases and moves across the resonant energy the sign of ϵ will change and the optical response will transition from transmissive to reflective or vice versa. This Fano resonant lineshape forms the backbone of the fitting equation and it is the resonant energy, E_F, that we hope to extract at each incidence angle.

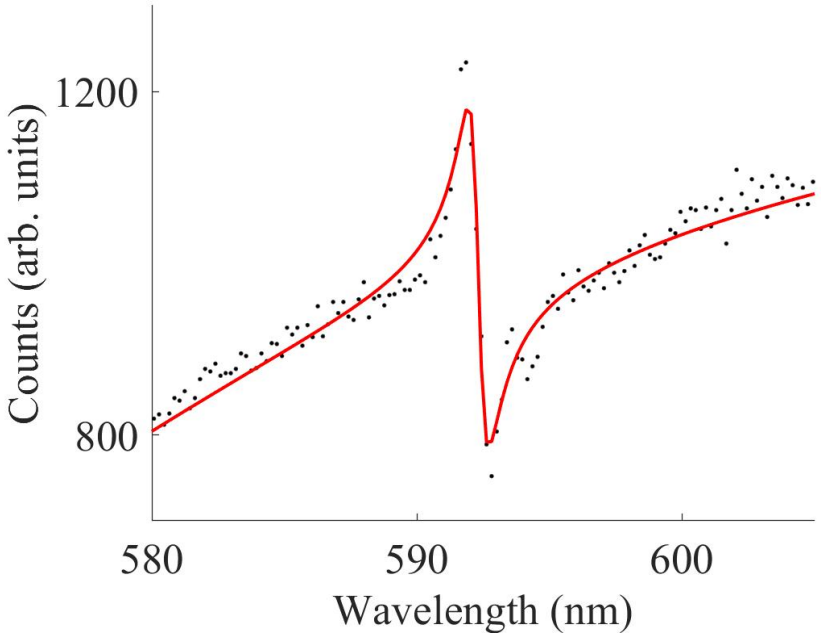

Figure 5.1: Characteristic experimentally measured spectral slice of a photonic band showing a spectrum exhibiting Fano resonance (blue dots) and its fitting function (red line).

Ultimately, to fit the spectral slices taken at each incident angle, several other background components must be added. An interference spectrum from various dielectric interfaces in the system will form the nonlinear background, while simple linear and constant background terms are also added to approximate wavelength dependence in the light source, optics, and detector. A typical fitting equation includes the Fano term and several background terms.

$$f(E) = A\frac{\left(\frac{2(E - E_F)}{\Gamma} + q^2\right)}{\frac{2(E - E_F)^2}{\Gamma} + 1} + B \times FP(E,t) + C \times E + D$$

where $FP(E,t)$ *is determined by an inverse matrix method with free parameter,* t

Equation 5.3: Fitting equation for experimental spectra as a function of energy, E, with parameters:

E_F – Fano-resonant energy
q – Asymmetry factor
Γ – Linewidth
A – Amplitude of Fano resonance
B – Amplitude of Fabry-Perot background
C – Linear background
D – Constant background

Fitting either the reflection or transmission intensity at a given angle with this Fano resonance equation thus gives the Fano-resonant energy of the photonic band at that point, and across all angles, reconstructs the photonic band. Fitting of all measured angles is accomplished by fitting the spectrum at the Γ point and iteratively fitting the spectra at angles out from the Γ point while propagating the fitted parameters as the starting point for the fitting algorithm on the next spectrum.

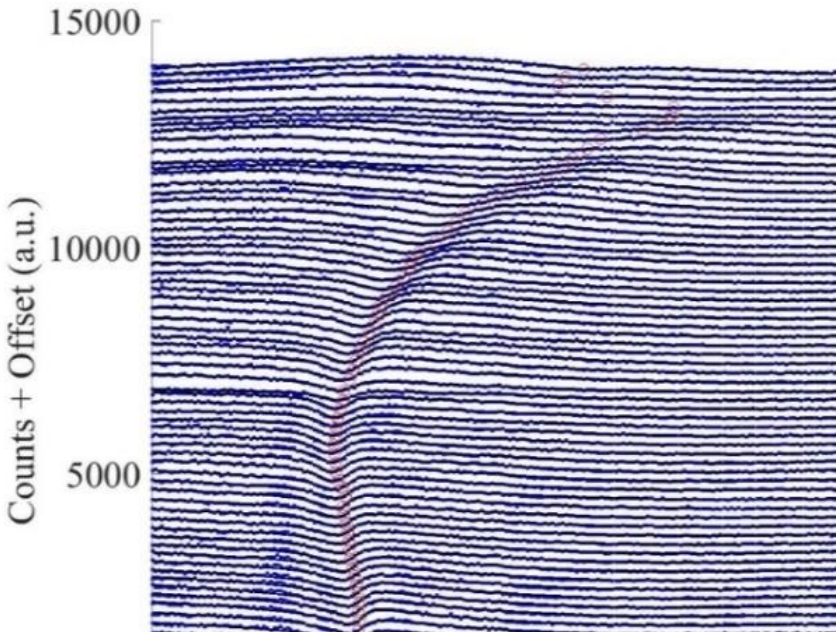

Figure 5.2: (Adapted with permission from C. Munley ACS Photonics SI). Demonstration of iterative fitting of Fano resonances to determine photonic band structure. Flat band spectra (blue dots) are iteratively fit, starting from the bottom at the Γ point with each subsequent spectra plotted with a vertical offset. The fit (black lines) are shown with the Fano-resonant energy highlighted (red circles).

5.2 Retrieval of Photonic Bands

While the fitting algorithm performs well on the simulated data, experimental results can result in significant noise in the set of fitted Fano resonances. If any fits completely fail due to missing resonance data (most likely the result of dust in the optical path), these points are excluded and the remaining Fano resonant wavelengths are connected by a robust Loess smoothing filter (Matlab 'rloess'). The final curves produced are used primarily as guides to the eye but also represent the numerically extracted curve from the measured Fano resonances. While peaks and dips may be the most obvious feature of a given spectrum, it is important to remember that the Fano resonance wavelength is often not located at a local extremum, so the fitted curves also serve to highlight the true photonic band, as opposed to the easily visible peaks and dips in reflection and transmission.

When examining two-dimensional photonic band structures, it becomes desirable to not only represent the one-dimensional reconstruction of a photonic band based on the measured or simulated reflection, but to synthesize a two-dimensional band structure based upon measurements of the band structure at various angles. A similar procedure to the one-dimensional case can be used here, where all of the extracted Fano-resonant wavelengths along with their excitation angles may be used with a two-dimensional Loess filter to produce a surface representing the smoothed band structure. This surface

will be quite sensitive to the angles of excitation sampled, so care must be taken to measure at appropriate angles to correctly sample the dynamics of the band in question.

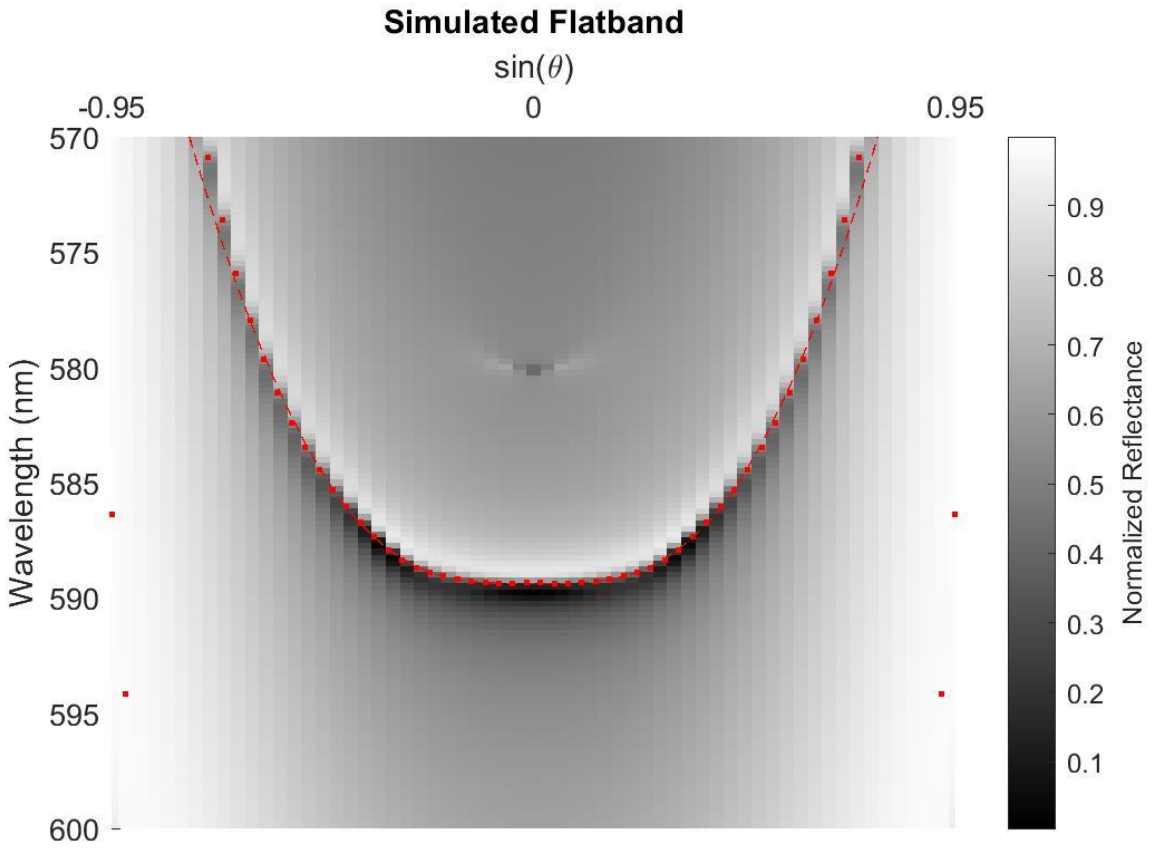

Figure 5.3: Demonstration of the fitting procedure and robust loess filter smoothing. The simulated flat band E-k spectrum is shown in black and white with fitted resonances plotted as red dots. The dashed red line represents the band structure fitting with a robust loess smoothing filter applied to the Fano resonant wavelengths. Note that the band itself is not the dip or peak of transmission or reflection but instead exists in between at the resonant wavelengths. Outside the primary fitting region, the extracted wavelengths of Fano resonances are spurious and excluded from the smoothing filter (red dots at edges of image).

6. 1-D Flat Band Design

A demonstration of a one-dimensional flat band serves as an important study of photonic band engineering. One-dimensionality here refers to the band remaining flat only along one axis in momentum space. In this section, the design and simulation of a metasurface exhibiting one-dimensional flat bands are presented.

6.1 Transitioning to the Visual Wavelength Regime

As a one-dimensional flat band had already been shown by H.S. Nguyen et al., the initial motivation to transition this design to the visible wavelength regime was to enable coupling with and dispersion engineering of visible light emitters. Nguyen's design consists of a vertically-symmetry-broken, period-doubled high contrast grating and demonstrates tuning of the band structure near the gamma point from a Dirac cone to a flat band and beyond to a W-shaped band [27]. In this design, the vertical symmetry breaking is introduced to couple the even and odd modes of the grating, and the period doubling is used to reposition the coupling point of these modes to the gamma point [27]. By adjusting the coupling between even and odd modes, the opposite dispersion trends from each mode can be made to cancel out, leaving a coupled mode with zero dispersion over a range of angles. Thus, the combination of vertical and lateral symmetry breaking results in a tunable photonic band at the gamma point, which can be fine-tuned into a flat band.

Although classical electromagnetic solutions remain scale invariant, the properties of materials do not. Most notably, silicon-on-insulator (SOI) wafers allow for the fabrication of high index contrast metaoptics for the near-infrared and infrared regimes but have significant loss in the visible regime. Typically, silicon nitride is the platform of choice for visible wavelengths, allowing for low loss albeit with smaller index contrast in a silicon nitride on silicon oxide platform. This is fine for metalenses, but the

lower index contrast presents a severe problem for the vertical-symmetry-broken flat band structures. With the refractive indices of silicon nitride and the underlying oxide layer remaining so close together, the fields that are designed to live at the boundary between silicon and oxide in the infrared design bleed much further into the oxide layer when the silicon is replaced with silicon nitride. This is a known issue for nonlocal visible metasurfaces, and splitting the difference by using silicon-rich silicon nitride has shown some promise in allowing for a high index contrast along with visible transmission [42]. Switching to patterning a gallium phosphide thin film, on the other hand, completely abandons CMOS compatibility in favor of the simplest solution from a theoretical perspective. Gallium phosphide has a similar refractive index to silicon and can be obtained as a thin film with silicon as a substrate. By undercutting the GaP via a selective isotropic etch of silicon, we can achieve the theoretical ideal of a high-index, visibly transparent material with only air above and below it.

Thankfully, our lab had previously developed a fabrication process for patterning and undercutting gallium phosphide on silicon chips and so this technique could be applied for the one-dimensional flat band. However, the partial etching necessary to provide vertical symmetry breaking in the flat band device presents a practical issue for fabrication. Like all fabrication parameters, the partial etching depth is subject to error during fabrication, but this error will be the same across the entire chip, so another parameter must also be used to fine-tune the curvature of the intended flat band. Thankfully, the fill factor of the device also allows for tuning of the band curvature. The

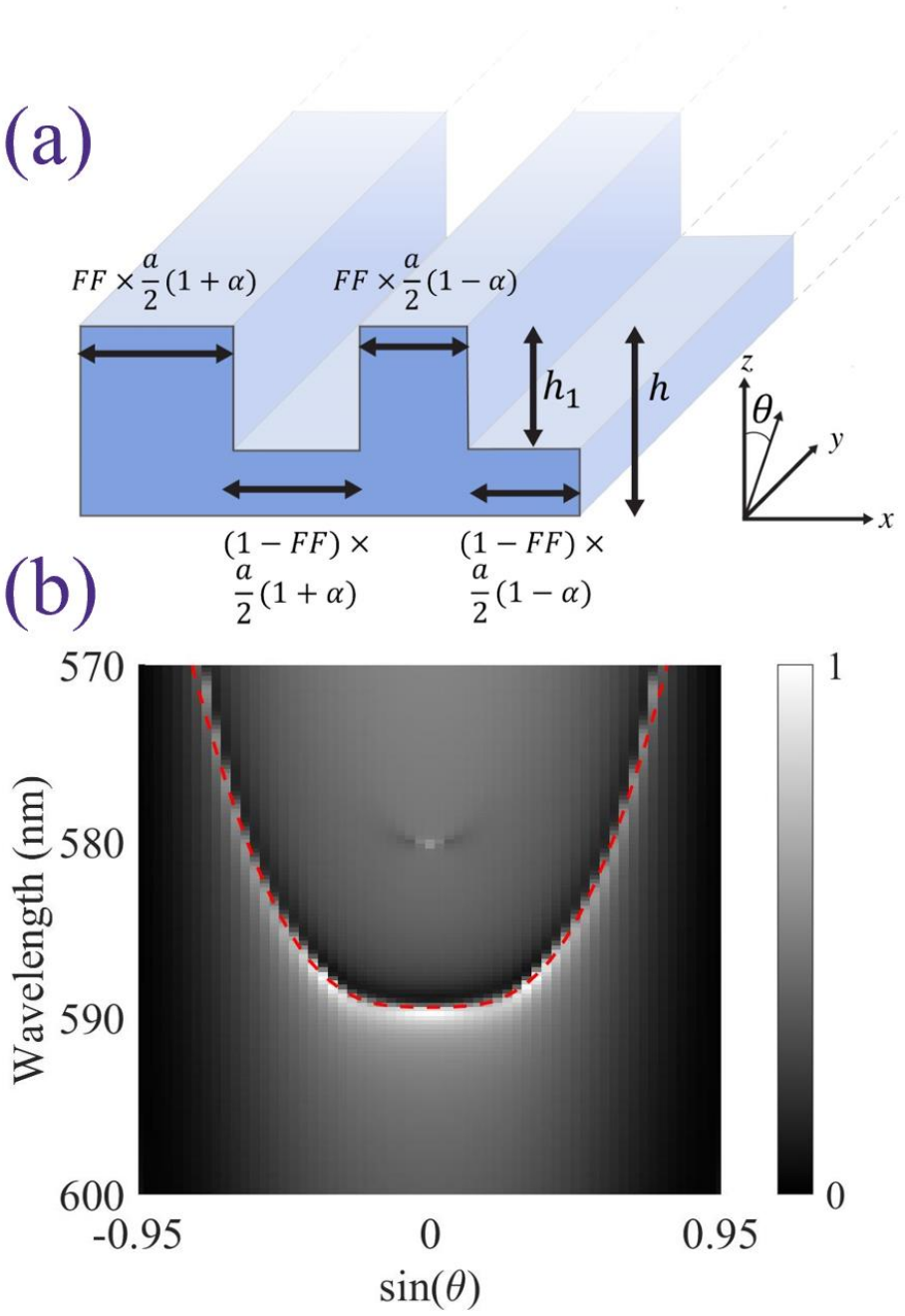

*Figure 6.1: (*Adapted with permission from C. Munley ACS Photonics) a) Design dimensions of the unit cell of the one-dimensional flat band, showing the parameters, a, the period, FF, the fill factor, α, the period-doubling asymmetry, the height, h, and the partial etch depth h_1. Note that the measured angle of the flat band, θ, is along the length of the bars. b) Simulated flat band dispersion from the designed metasurface.

targeted partial-etch depth was determined so that the fill factor would be fifty percent

to allow for maximal tuning of the band. In addition to being flat, in order to couple with a given quantum emitter, the wavelength of the photonic flat band must also be on resonance with the emitter. To accomplish both goals even in the presence of fabrication disorder, an array of devices with varying parameters is created so that even with random error in the partial etch depth, one of the devices will most likely be a flat band at the correct wavelength. The array of different devices also allows for measurement of the tuning of the flat band and easier identification of the band of interest.

6.2 Dimensions of the Design

The final device was fabricated on a piece of a wafer purchased from NAsP III/V GmbH consisting of a 210nm thick GaP thin film grown via chemical vapor deposition (CVD) on a silicon substrate. A 400nm spin-coated film of Zeon ZEP 520A was patterned with 100kV electron beam lithography (EBL) using a JEOL JBX6300FX. Reactive ion etching (RIE) was used to partially etch the GaP at an estimated rate of 4 nm/s. The mask was then re-exposed with EBL and portions of the GaP were completely etched using RIE to expose the underlying silicon substrate around the metasurface area. Xenon difluoride was then used to selectively remove the silicon substrate, undercutting the GaP and leaving it floating, suspended by unetched GaP support beams. After dissolution of the mask, the array of metasurfaces was complete. In the final fabricated device, the partial etching ended up being 182nm, the period was 436 nm, and the period-doubling asymmetry was .1. It is worth noting that with a partial etch of 182nm, the thinnest part of the floating GaP membrane is only 28nm thick, however, the one-dimensional nature of the device means that the bars composing the metasurface completely span the device and support it. The fragility of the partially etched layer of the floating GaP metasurface becomes a more serious issue when fabricating a two-dimensional metasurface.

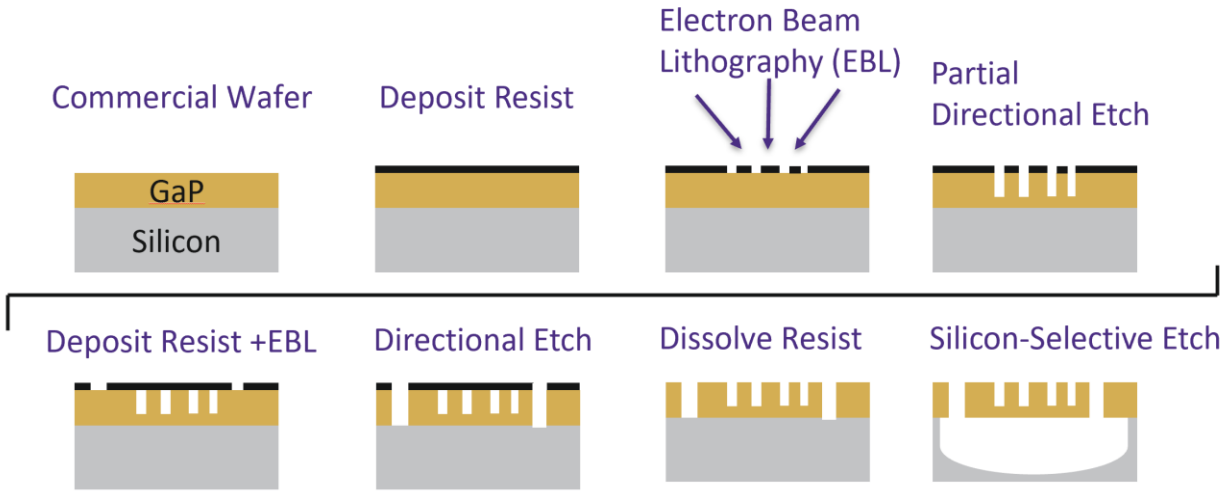

Figure 6.2: Illustration of the steps of fabrication for the suspended GaP membrane structure. Resist is deposited and subsequently patterned via electron beam lithography. After calibration of the etch rate, a directional etch is applied to partially etch the GaP membrane in order to create vertical-symmetry-breaking in the structure. After the directional etch and dissolution of the first resist mask, a second round of resist, patterning and directional etch is performed to open trenches down to the silicon substrate around the metasurface. In between these trenches, patches of unetched GaP are left to support the soon-to-be-floating metasurface. Finally, a silicon-selective isotropic etch is used to dissolve the underlying silicon substrate, leaving the metasurface floating.

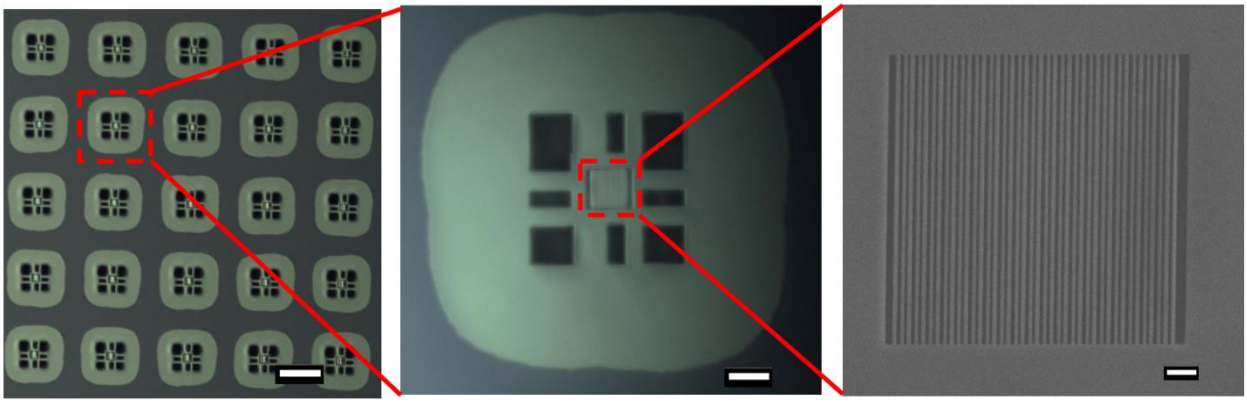

Figure 6.3: (Adapted with permission from C. Munley ACS Photonics). Visible and electron microscopy images showing the array of device, the flat band device, and a scanning electron microscope image of the details of the device. From left to right, scale bars are 50um, 10um, and 1um.

7. 1-D Flat Band Results

Using the technique of energy-momentum spectroscopy, the measured band structures from the one-dimensional flat band metasurface were found to agree well with simulations. Across the array of devices, evolution from flat bands to a multivalley band was seen, as expected. As previously discussed, a background-aware iterative fitting method was applied to extract parameters for the Fano resonances and the photonic bands.

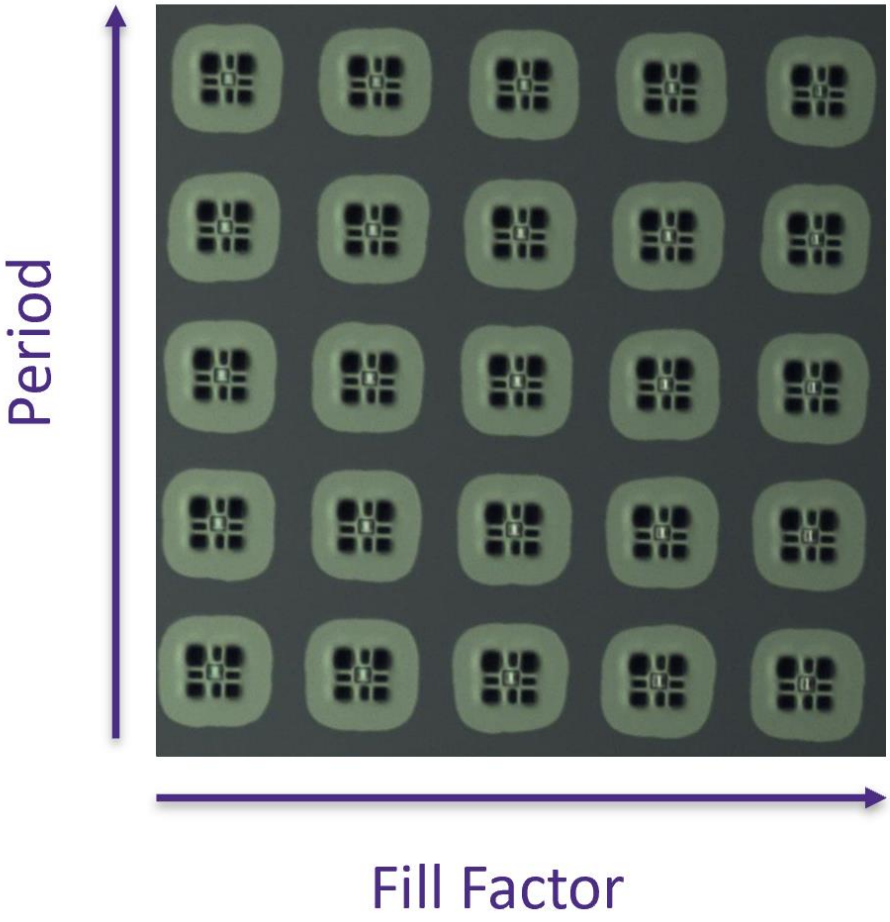

Figure 7.1: Image of the fabricated chip showing floating GaP membrane metasurfaces with a fabricated array varying in period and fill factor to account for fabrication error.

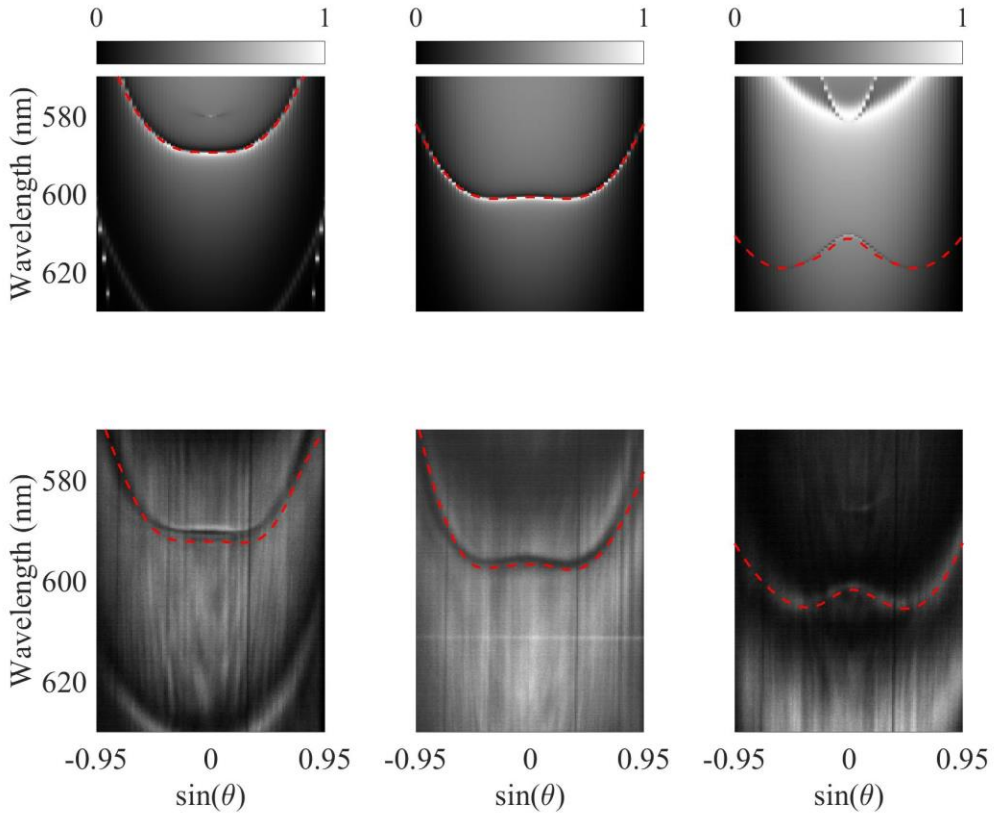

Figure 7.2: (Adapted with permission from C. Munley ACS Photonics) Simulated (top) vs measured (bottom) E-K spectra with extracted photonic band fits (red dashed line) showing the evolution from a flat band to a multivalley band.

7.1 Integration of Material

Given that the motivation to extend this photonic flat band into the visible regime was originally to demonstrate compatibility with visible emitters, it made sense to pair a visible emitter with the flat band metasurface and measure the photoluminescence. With the flat band presenting at ~600nm, it matched well with a materials platform we had previously been exploring: CdSe nanoplatelets (NPL). Nanoplatelets are small crystals with an atomically precise number of layers in one dimension and a varying lateral size. Specifically, their narrow, atomically precise dimension leads to a specific energy for excitons in these materials, while their lack of lateral confinement avoids the three-dimensional exciton confinement of quantum dots which so often leads to inhomogeneous broadening. In this way, they can be thought of as a sort of "diced quantum well" that can be applied to a device or substrate via spin-coating, avoiding the laborious growth and lattice matching which an integrated quantum well would require.

The six monolayer CdSe nanoplatelets used were fabricated by the Cossairt Lab at UW with a modified direct synthesis developed by Cho et al. [43]. While different species representing the number of atomic layers in the nanoplatelet are created, separation of the nanoplatelets by species can be accomplished with a centrifuge. The six-monolayer species has a main emission peak at 585nm with a full width at half max of 10.1nm. A representative survey of the solution measured with transmission electron microscopy shows overall dimensions of 1.9nm for the six-monolayer height, and rectangular lateral dimensions varying from 10nm to 40nm. While the floating gallium phosphide membrane is quite thin, spin coating of the membrane does not break the membrane and instead led to a coating of the nanoplatelets spread across the chip.

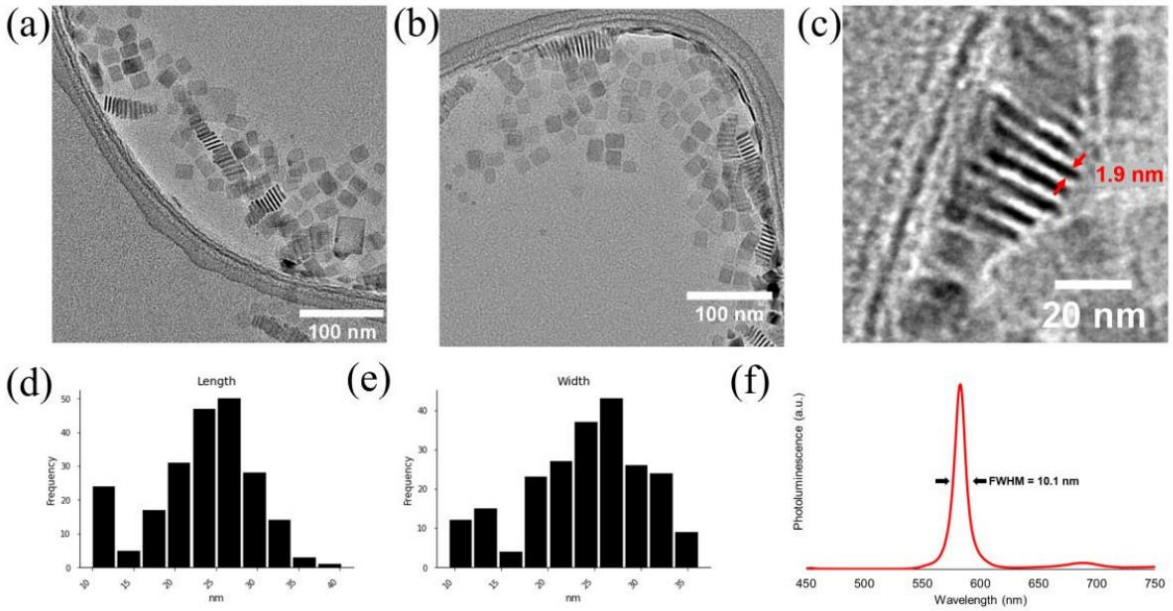

Figure 7.3: (Adapted with permission from C. Munley ACS Photonics SI) a), b), c) TEM images of a representative CdSe nanoplatelet suspension with callout of measured six monolayer thickness. Note homogeneity of NPL thickness and inhomogeneity in lateral dimensions. d), e) Histogram of the measured lateral dimensions of the NPL. f) Measured photoluminescence spectrum of a CdSe NPL sample without flat band device. Main peak with full-width at half-max shown as 10.1nm and note a much smaller peak that derives from the impurity species of seven monolayer-thick CdSe NPL.

After spin coating the device with nanoplatelets, the photonic band structure was measured again by using photoluminescence to probe the coupling between the CdSe nanoplatelets and the metasurface. Exciting above band gap, uncoupled photoluminescence is observed to dominate the spectrum, but energy-momentum spectroscopy can be used to observe emission into the flat photonic band. Because the band is flat over a range of angles, the spectrum over this range can be integrated to produce a spectrum that displays both the uncoupled photoluminescence peak and the flat-band-coupled photoluminescence. In this way, over a range of angles of emission, the effective photoluminescence is engineered to be bimodal, and enhancement of the emission at the flat band wavelength is demonstrated. The substantial portion of uncoupled photoluminescence is most likely due to the flat band mode residing mainly

within the dielectric structure of the GaP and the random nature of spin-coating—many of the nanoplatelets are likely not located within the band's field extent and thus do not experience coupling. It may also be observed that the emission of these uncoupled nanoplatelets is slightly stronger at larger emission angles. This is due to the natural dipole emission of the CdSe nanoplatelets combined with their proclivity to rest on their flat side when randomly deposited. With more precise deposition techniques, a larger portion of coupled material could most likely be realized.

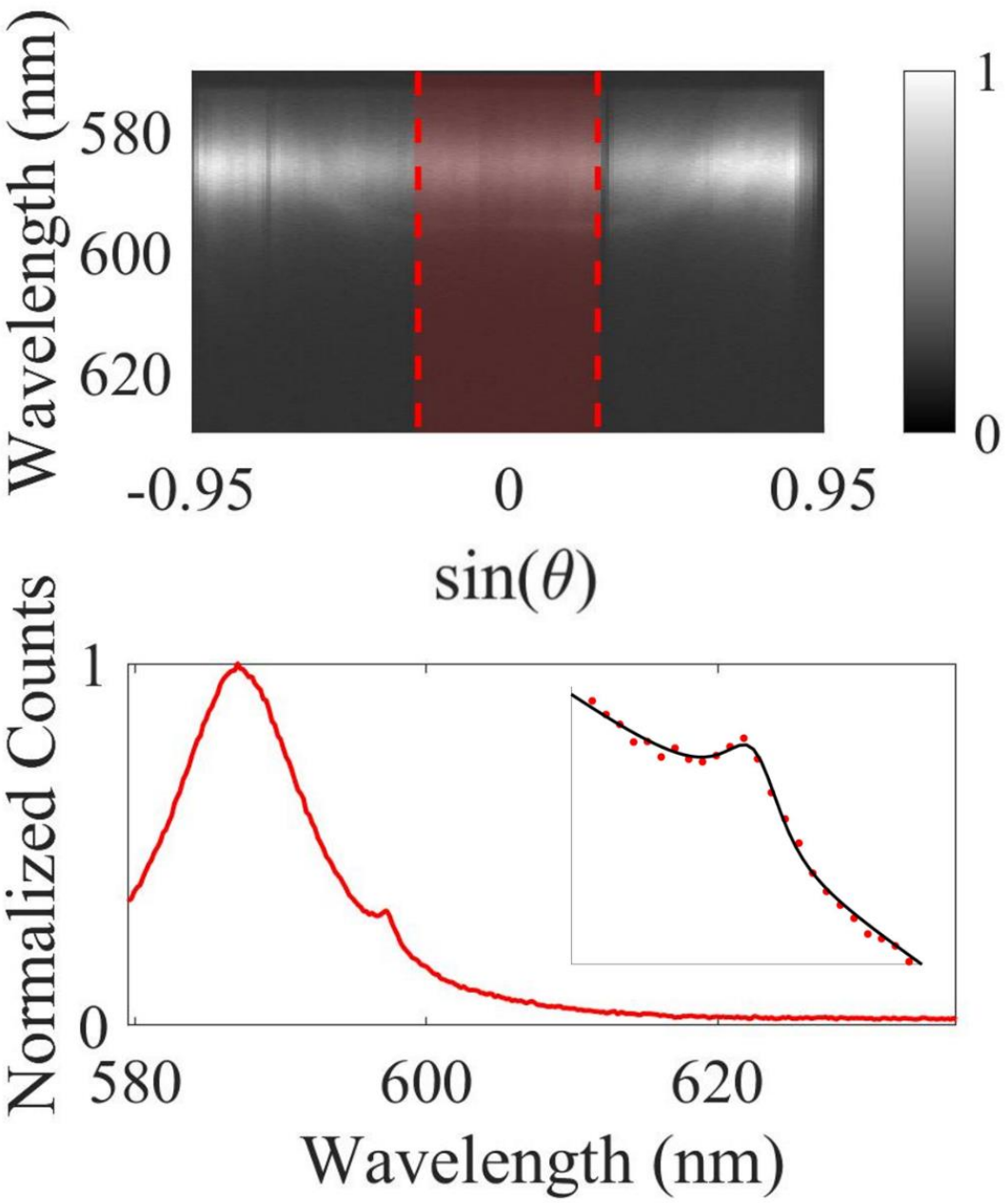

Figure 7.4: (Adapted with permission from C. Munley ACS Photonics SI): Full energy-momentum spectroscopy of the photoluminescence of CdSe nanoplatelets on the GaP flat band metasurface (top) along with an integration of the red-highlighted portion to produce a one-dimensional spectrum showing enhancement of emission at the flat band wavelength (bottom).

8. 2-D Flat Band Design

Transitioning from one to two dimensions is certainly not a trivial process—for many physical processes, behavior can be completely different and, in some cases, even limited to specific dimensionalities. Thankfully, photonic flat bands have been previously demonstrated in two dimensions as arrays of laser-written waveguides and in plasmonic systems as discussed earlier, so it is unlikely that there are fundamental barriers to the realization of a metasurface with two-dimensional photonic flat bands. To start we should probably confirm that the one-dimensional flat band is not accidentally a two-dimensional flat band. Simulating across the other axis of the one-dimensional flat band structure shows that the resulting band structure displays highly dispersive modes that are almost as far away as possible from a flat band. Evidently, there is a lot of work to be done! Here I will walk through the evolution of the one-dimensional flat band design to the two-dimensional flat band design, starting with a consideration of the symmetries of the problem at hand.

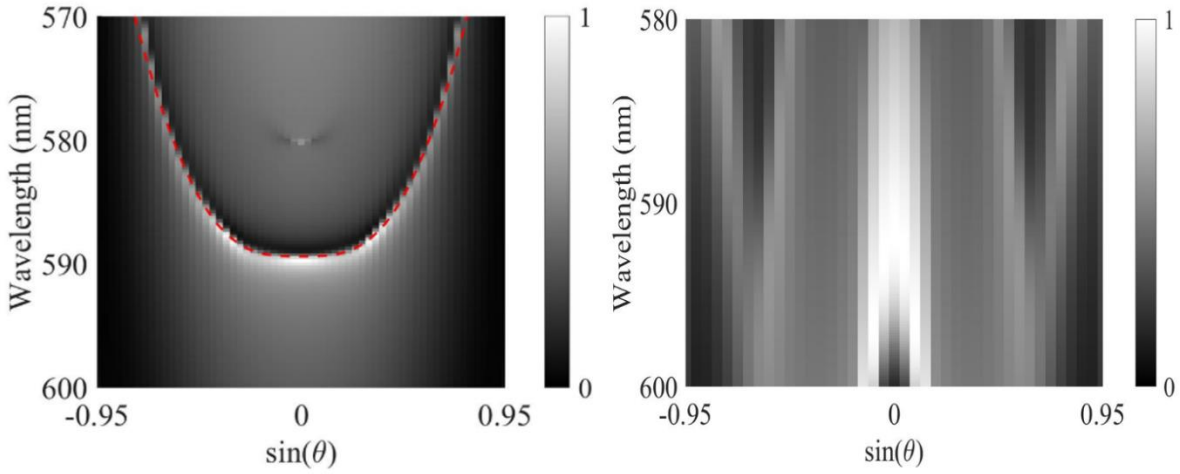

Figure 8.1: Verification that the one-dimensional photonic flat band is not accidentally a two-dimensional photonic flat band! Dispersion along y-axis with P-polarized light (left) is locally flat near the Γ point with the fit flat band shown (red-dashed line), while dispersion along the x-axis with P-polarized light (right) shows significant dispersion in the vicinity of the Γ point.

8.1 Consideration of Symmetry

In one dimension, creating flat bands from a lithographically defined lattice was an exercise in generating a non-intuitive cylindrically symmetric optical response counter to the layered nature of the material to be patterned. In two dimensions this same behavior holds, but in addition the necessary spherical symmetry of a two-dimensional flat band is in tension with the translational symmetry of the lattice. However, if we require a band that is locally flat in all directions around the gamma point in two dimensions, it is automatically true that the flat band is polarization insensitive at that point, as the rotation of the polarization is equivalent to the rotation of the lattice. Here, the polarization symmetry can be intuitively implemented by enforcing a fourfold symmetry to the lattice and unit cell. To obtain band tuning, a bipartite lattice is desired in order to independently tune the modes of multiple sublattices, and it is this desire for a fourfold symmetric bipartite lattice that makes the Lieb lattice a reasonable place to start. While the original investigation by Lieb into bipartite lattices is agnostic to any specific tiling symmetries, here, we refer to that fourfold square tiling bipartite lattice commonly understood to be the "Lieb" lattice, as opposed to the "Kagome" lattice [44].

In order to preserve strong visible-regime transmission, the first design approach was to adiabatically transition the gallium phosphide one-dimensional flat band lattice into a two-dimensional lattice. First, a square two-dimensional unit cell was defined with the same width as the one-dimensional unit cell. Splitting the bar elements to create four rectangular meta-atoms per unit cell allows for the beginning of a transition to two dimensions. This increase in the number of meta-atoms introduces additional bands, but does not destroy the original one-dimensional flat bands, only perturbing them. By reducing the vertical scale of these four meta-atoms we can begin to bring the unit cell towards the desired four-fold symmetry. Upon reaching the necessary vertical scale for a square larger element, the smaller elements are also transitioned to a square aspect ratio.

This results in a two-dimensional array of meta-atoms but does not retrieve the desired four-fold symmetry to demonstrate flat bands along multiple directions. Thus, the two dimensional array of meta-atoms is transitioned to a Lieb lattice wherein one larger square meta-atom is retained, with two smaller square meta-atoms surrounding it, and the final meta-atom element reduced to nothing.

While this approach proved fruitful in simulation, realization of the device as a floating gallium phosphide membrane was quite difficult. Without the one-dimensional elements spanning across the partially etched region, the metasurface became a 10-20nm thin film spanning a 40-micron gap while supporting thousands of 200nm-thick meta-atoms. In preliminary designs, significant buckling of the film was observed, and in subsequent designs to correct this issue, the feature size of the pattern was too difficult to pattern with the thickness of resist required. Additionally, as many applications of the two-dimensional flat band device would rely on transmission, the undercut gallium phosphide structure would be an unsuitable platform as the isotropic silicon undercutting etch results in a non-uniform surface underneath the gallium phosphide membrane. For these reasons, the design was transitioned to a crystalline silicon on sapphire platform, which allows for transmission and substrate support of the device, although full visible regime operation is no longer feasible.

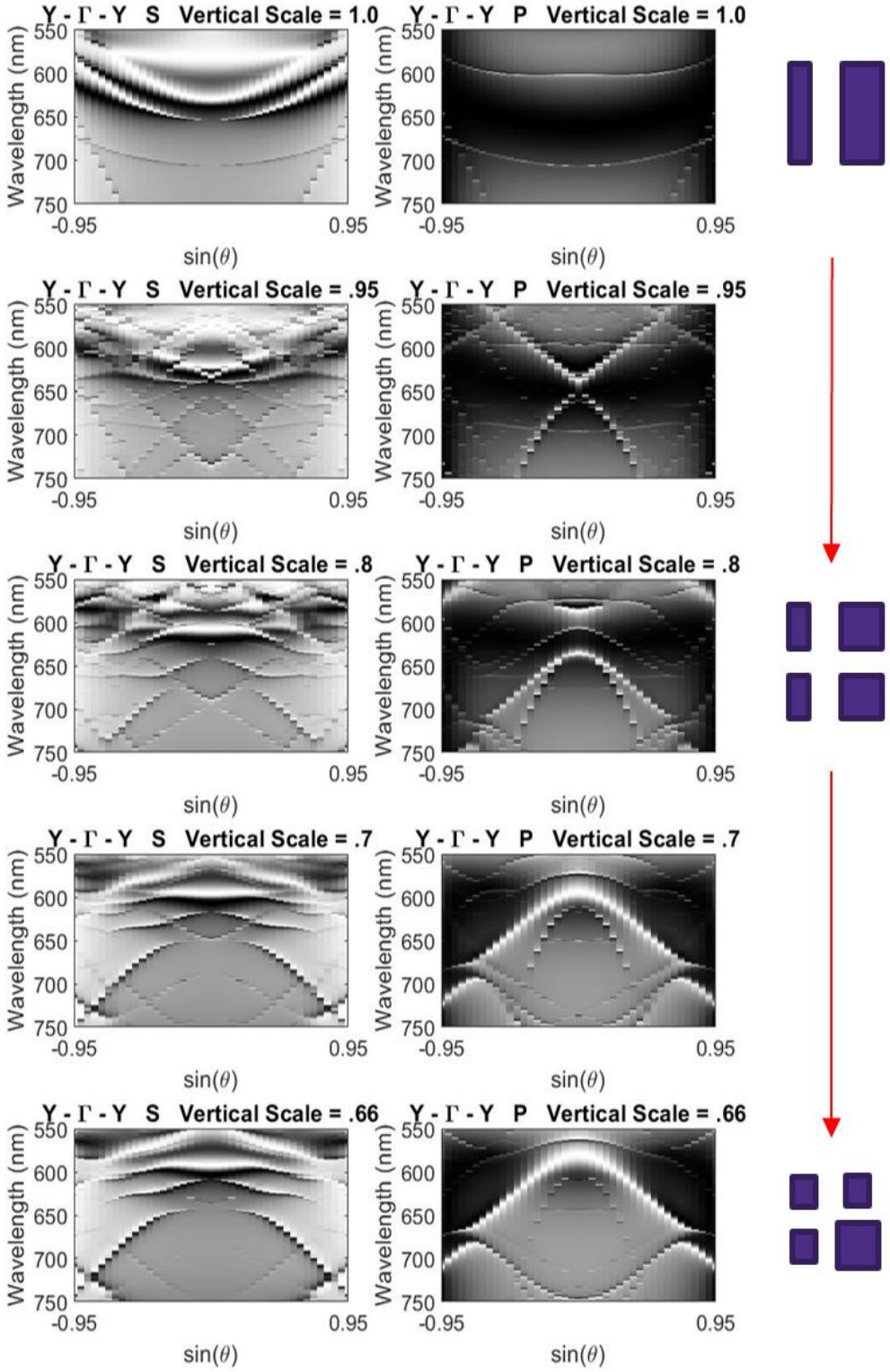

Figure 8.2: Photonic band structure evolution from the one-dimensional flat band structure to a two-dimensional lattice of square resonators, shown as a function of the vertical scaling factor applied to the height of the one-dimensional bar elements.

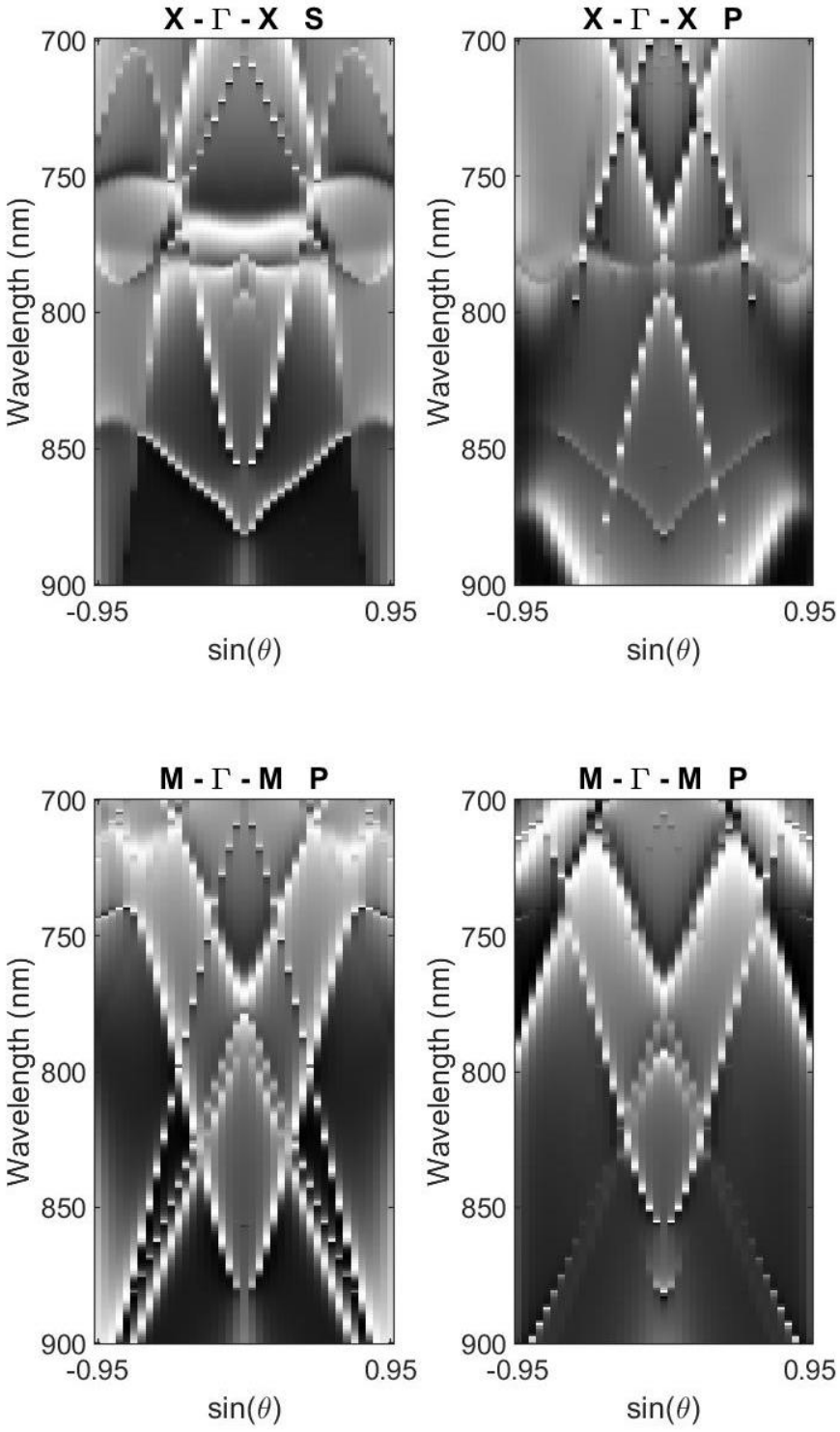

Figure 8.3: Band structure of a square-element Lieb lattice optimized for flat bands along the X axis of the band structure in both polarizations. However, note the extremely dispersive bands along the M axis, indicating these flat bands do not extend across momentum space in two dimensions.

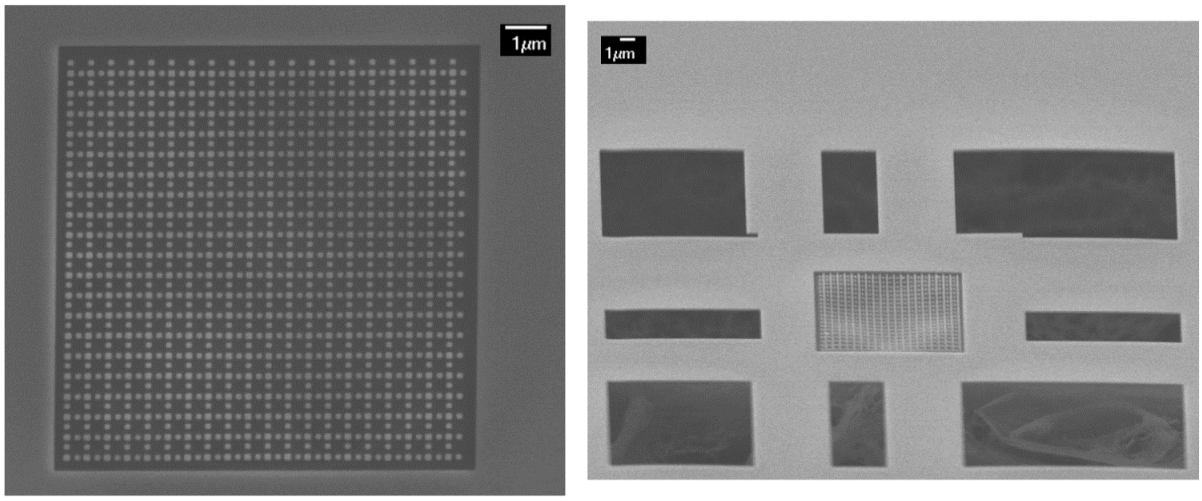

Figure 8.4: Scanning electron microscopy images of the suspended GaP Lieb metasurface based on a lattice of square posts. Top-down view (left) showing a large number of small elements, and an oblique view (right) where the beginning of buckling can be seen in the gallium phosphide membrane. Beneath the floating membrane the rough surface of the undercut silicon can be seen.

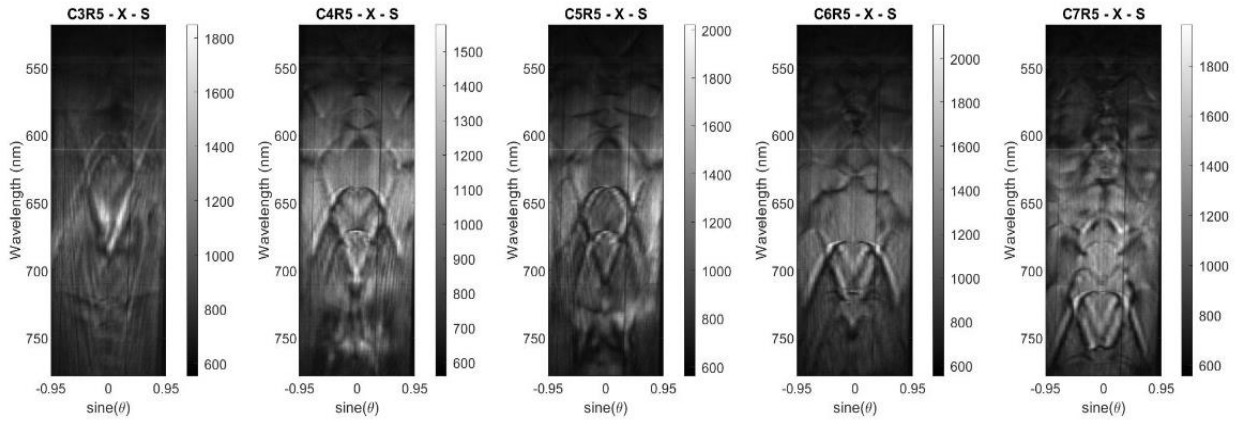

Figure 8.5: Experimentally measured photonic band structure along the X axis of the Brillouin zone with S polarization as a function of fill factor across multiple devices. Starting from lowest fill factor (C3R5), the devices transition to nominal fill factor (R5C5), and finally to highest measured fill factor (C7R5). Colorbars showing counts (arbitrary units) are displayed next to each measured band structure. The resolution of the bands is quite low, most likely due to fabrication disorder.

8.2 Holes in Crystalline Silicon

Design for the crystalline silicon Lieb lattice started from a design based on holes in a film of silicon, as opposed to posts. The symmetries here are the same, and it turns out that much of the same mode structure is observed, as well. Recently, this quasi-Babinet principle has been identified and used to link the behavior of post-based and void-based metasurfaces [45]. A naïve Lieb lattice photonic crystal with circular holes displays several modes. Starting from the fundamental, the symmetry of the modes can be assessed by looking along the X and M axes in momentum space. Bands with specific symmetries along the major axes of the Brillouin zone are often limited to being flat along only those axes, but as the energy increases, we find the lowest energy band that has similar curvature when measured along all major axes. Instead of fighting the symmetries of the bands by transitioning a band that is originally flat along only one axis, this is the band we will transition into a flat band.

By tuning the partial etching parameters, we can transition the Lieb lattice of circular holes into a flat band, with the band still touching the band above it. This results in the correct flat band dispersion but has a rather low quality factor and small numerical aperture. Experimentation with the structure is rather limited, as to preserve the necessary symmetries. However, by changing the eccentricity of the linking elements of the Lieb lattice, we can demonstrate gapping of the flat band from higher-energy bands and an increase in quality factor. Further increase in the eccentricity continues to increase the quality factor and wavelength-selectivity of the band, but eventually leads to band bending and unavoidable coupling between the two elliptical elements. It is also desirable that the flat photonic band remain broad enough to span any deviation from a perfectly flat dispersion.

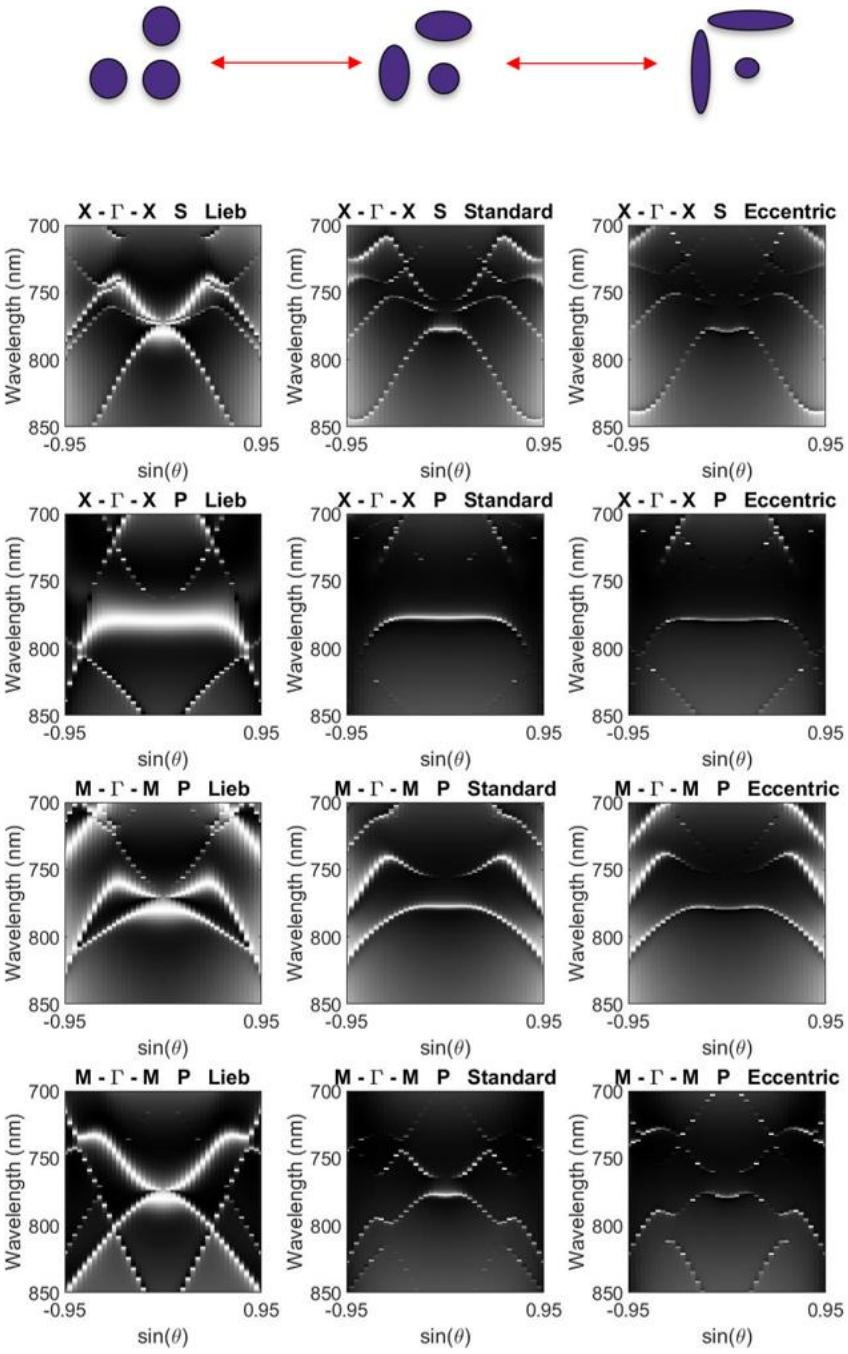

Figure 8.6: Comparison of band structure as a function of eccentricity of the linking lattice elements showing X and M momenta axes and S and P polarization axes. While the flat band in the Lieb lattice (left) touches other bands, the band is shifted away from its neighbors as the eccentricity increases to the fabricated "standard" (center). As the eccentricity further increases the band dispersion itself changes, shifting to a multivalley dispersion (right). Note that as the eccentricity of these elements increases, the band in question also narrows showing an increase in the quality factor of its resonance.

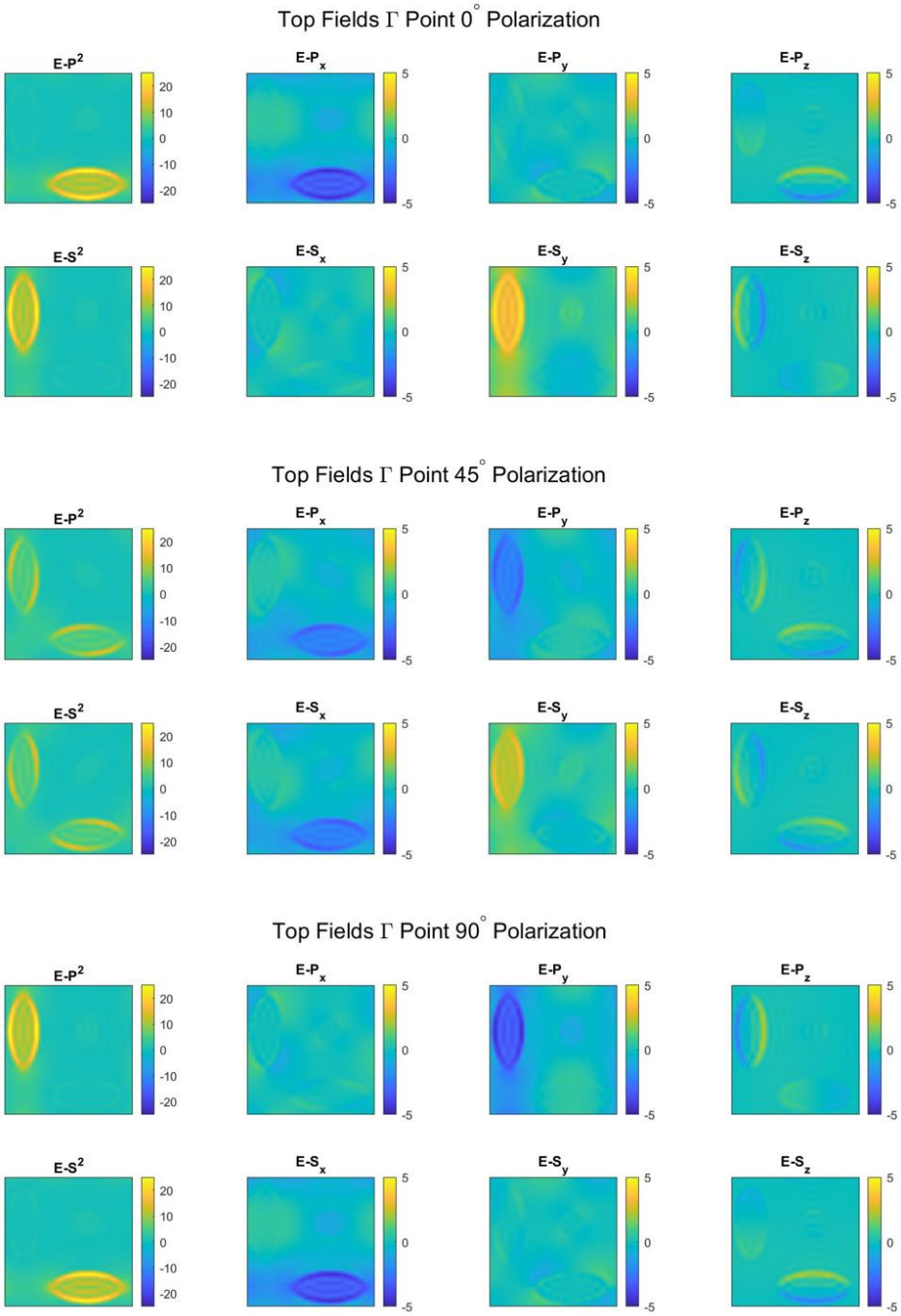

Figure 8.7: Field profiles and intensities for various incoming polarizations at the top of the metasurface at the air-silicon interface. Here, E-P^2 is the intensity due to P-polarized input light with field components E-P_x, E-P_y, and E-P_z. Similarly, E-S^2 is the intensity for S-polarized input light with field components E-S_x, E-S_y, and E-S_z.

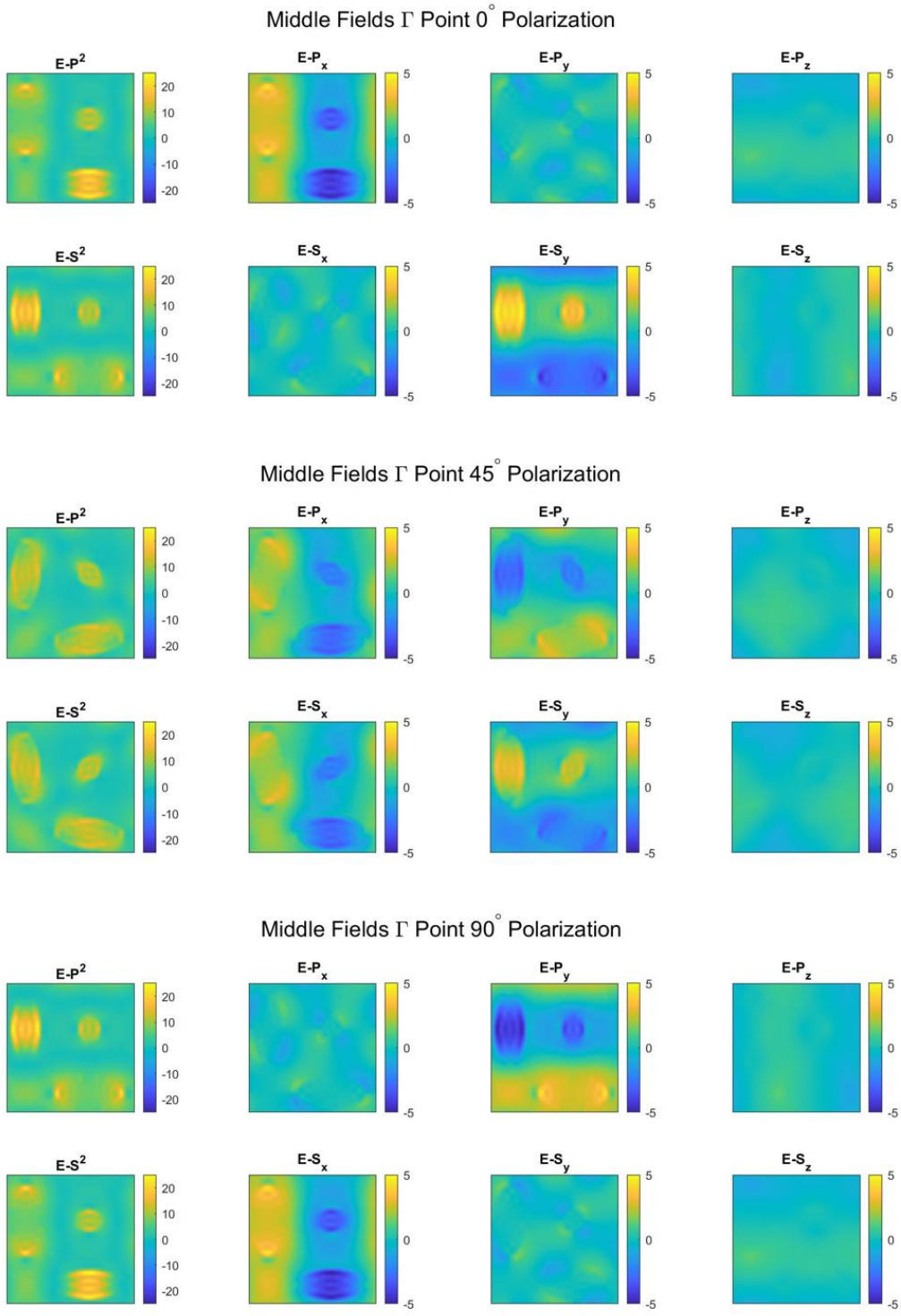

Figure 8.8: Field profiles and intensities for various incoming polarizations in the middle of the partially etched silicon metasurface. Here, E-P^2 is the intensity due to P-polarized input light with field components E-P_x, E-P_y, and E-P_z. Similarly, E-S^2 is the intensity for S-polarized input light with field components E-S_x, E-S_y, and E-S_z.

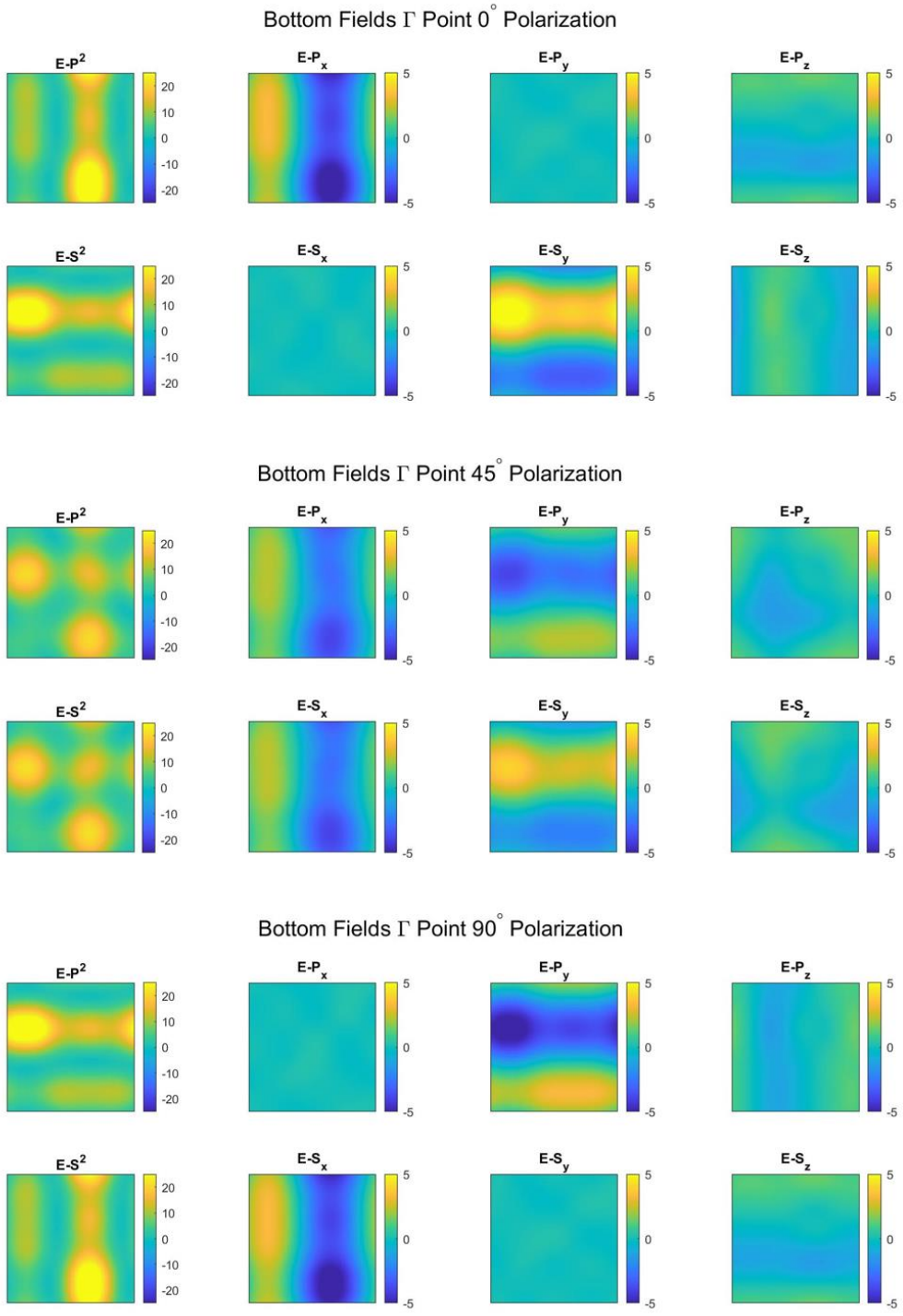

Figure 8.9: Field profiles and intensities for various incoming polarizations at the bottom of the metasurface at the silicon-quartz interface. Here, E-P^2 is the intensity due to P-polarized input light with field components E-P_x, E-P_y, and E-P_z. Similarly, E-S^2 is the intensity for S-polarized input light with field components E-S_x, E-S_y, and E-S_z.

8.3 Fabrication Considerations

With the flat band identified, focus turns to faithfully fabricating this design. A study of the partial etch depth shows a similar dependence to the one-dimensional flat band with a transition from parabolic dispersion to a multivalley dispersion with flat band dispersion identified in the middle. Similar to the one-dimensional case, lateral parameters can also be used to tune the dispersion. As in the one-dimensional case we again use a sweep of lateral parameters to compensate for anticipated error in the partial etching depth, allowing for fabrication of the flat band device even in the presence of fabrication disorder.

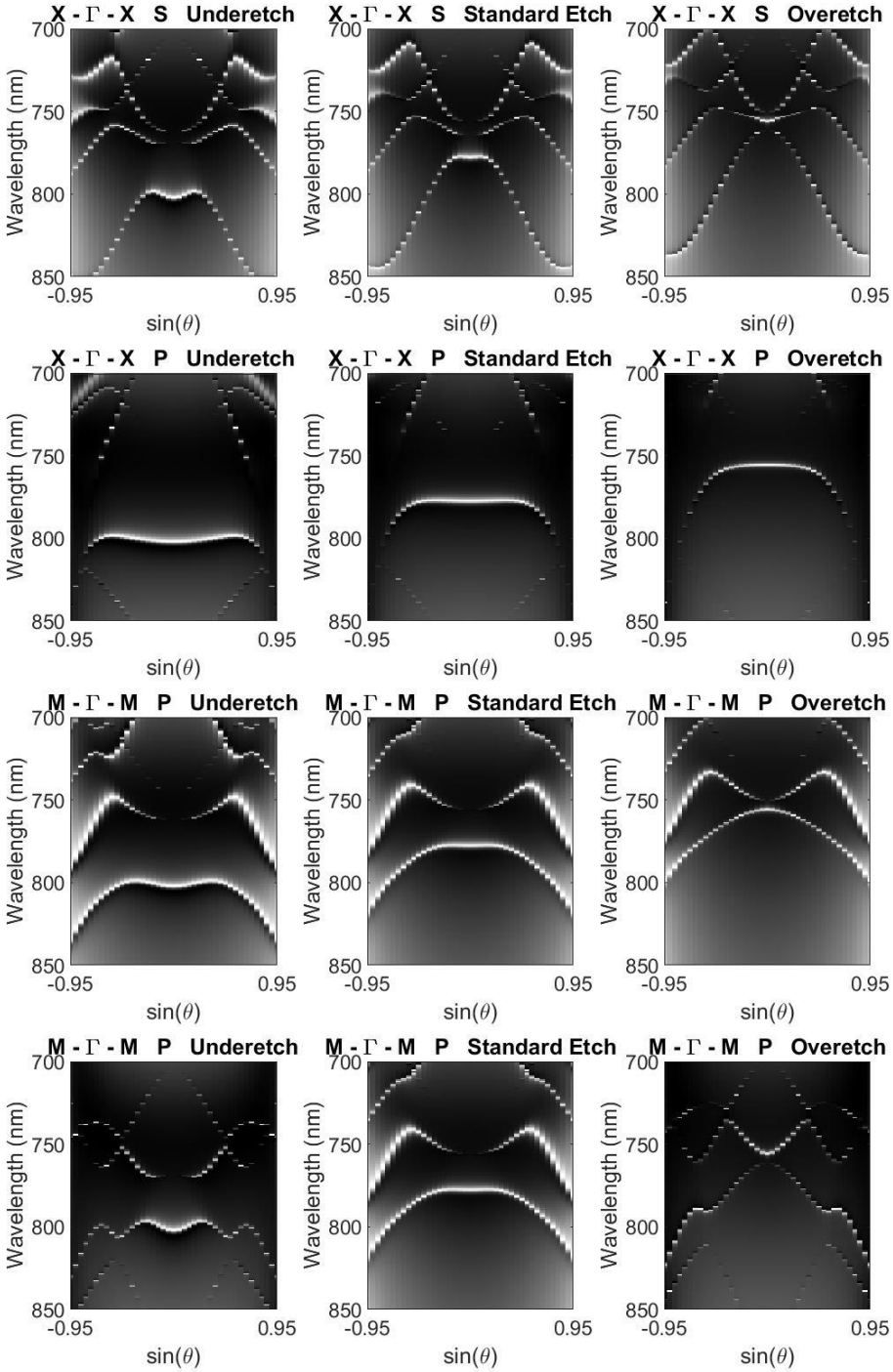

Figure 8.10: Study of etch dependence of two-dimensional flat band structure showing X and M momenta axes and S and P polarization axes. The band structure of the intended "standard" partial etch depth is shown (center), along with variation in the partial etch depth showing under etching (left) and over etching (right). Note correlated transition from multivalley dispersion to parabola as the partial etch depth changes.

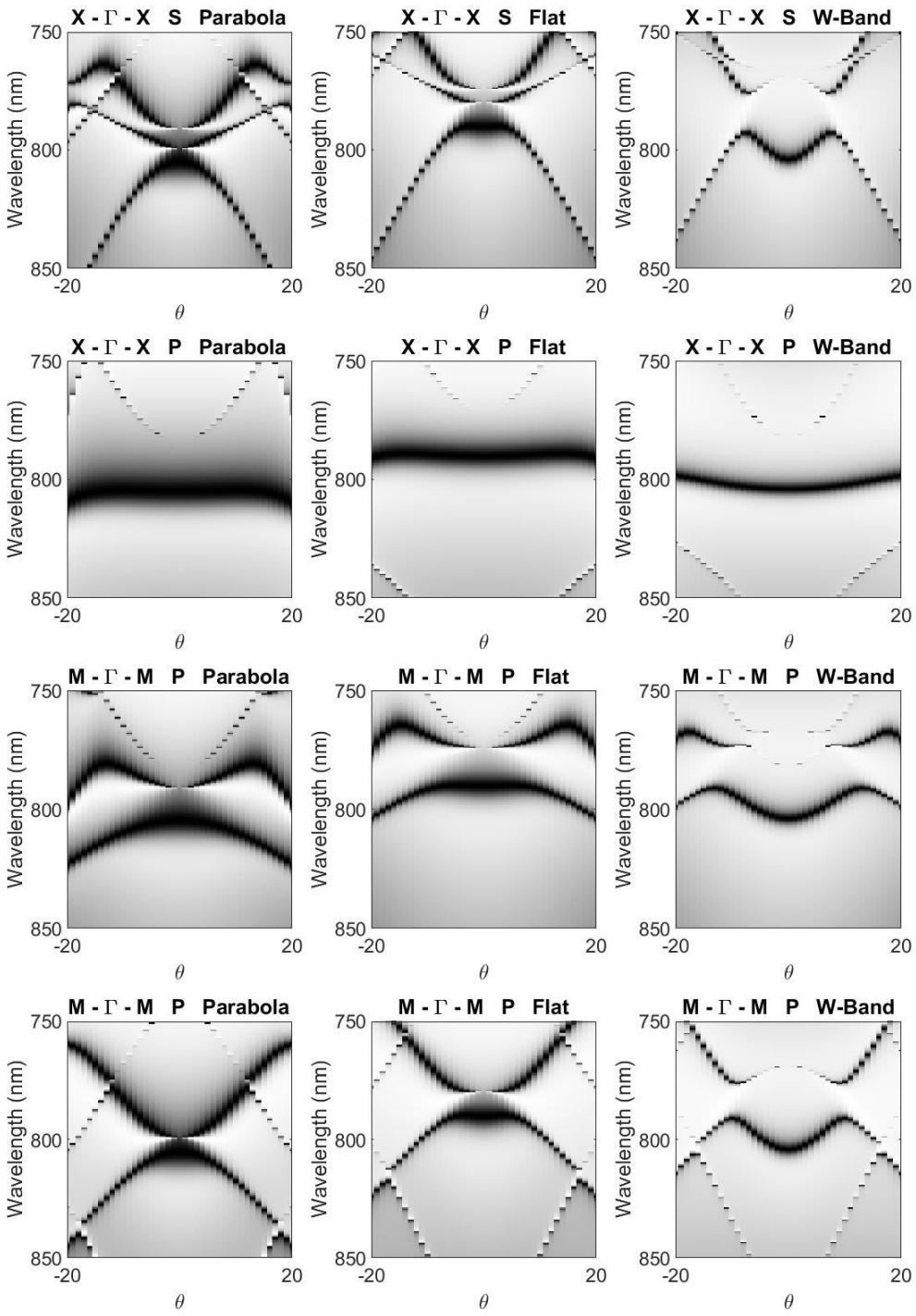

Figure 8.11: Study of the photonic flat band's dependence on fill factor showing X and M momenta axes and S and P polarization axes. The band structure of a flat band is show (center) along with parabolic (left) and multivalley or "W band" dispersion (right) effected by a change in fill factor. Note again that the transition in dispersion is seen along all Spectra here are shown in transmission.

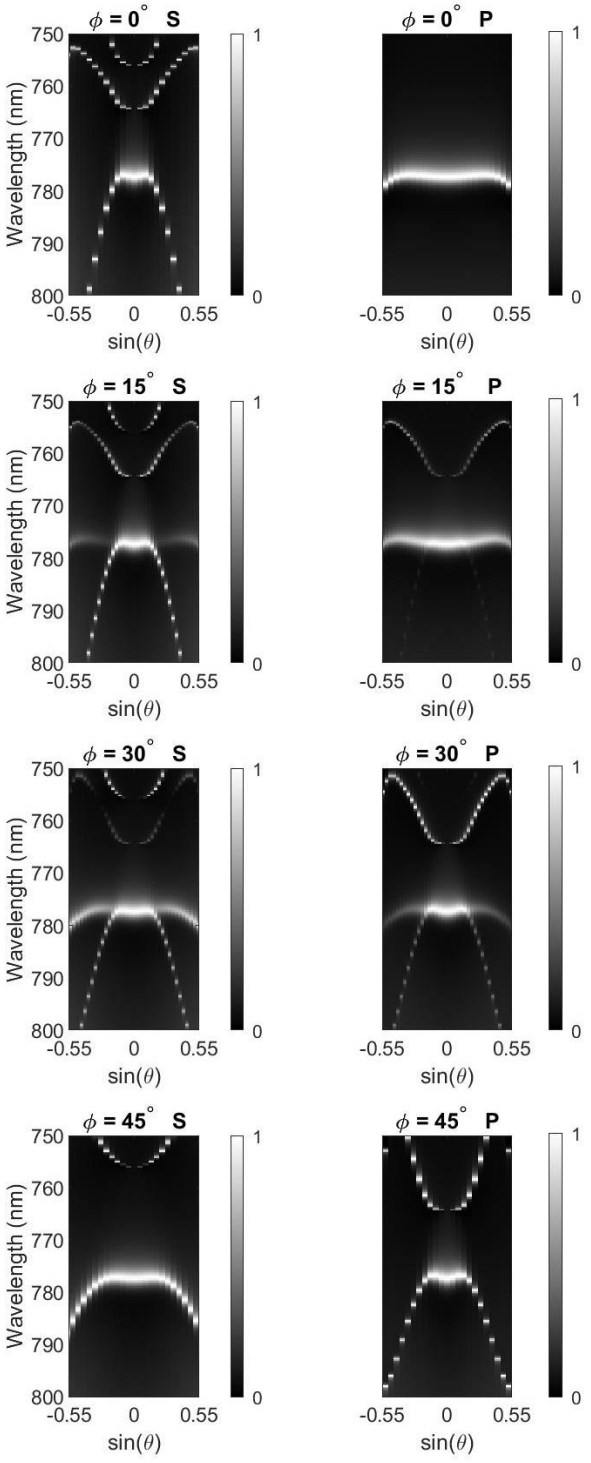

Figure 8.12: Simulated band structure of the flat band metasurface along 15-degree rotational steps in azimuthal angle from along the X axis is in the Brillouin zone (ϕ = 0°) to along the M axis (ϕ = 45°) for both S and P polarizations.

9. 2-D Flat Band Results

Measurement of the two-dimensional flat band device is accomplished in much the same way as in the one-dimensional case; however, measurements must be repeated for various axes in momentum space. Measuring along these different axes in energy-momentum spectroscopy requires a relative rotation between the spectrometer slit and the back focal plane as re-imaged onto it. Sadly, the spectrometer is not easily rotated (especially do not attempt this if your spectrometer's CCD is cooled cryogenically!), so rotation of the measured back focal plane of the objective must be accomplished by either rotating the optical field or rotating the sample itself. Rotation of the optical field can be accomplished through insertion and rotation of a Dove prism, but the additional optical path length added with the Dove prism would require a rebuild of the entire system and the Dove prism rotation axis would have to be precisely aligned with the optical measurement axis. Rotation of the optical field also includes the pitfall of introducing different polarizations to the optical system which may have slightly different efficiencies throughout the system. Instead, the sample is simply placed on a rotating stage so that the relative orientation between the metasurface axes of symmetry and the rest of the microscope can vary. In this manner, the microscope elements and associated polarizations can remain constant while only the sample is changed. Measurement at each axis is accomplished by rotating and re-centering the metasurface of interest.

9.1 Comparison with Simulation

The measured flat band results are seen to agree well with the simulated E-k spectra. The main issue in measurement while rotating the sample is keeping the orientation of the metasurface normal to the exciting axis of the objective. As can be seen in the measurement, asymmetries in the measured band structure can present due to the sample being tilted. While the sample may initial be correctly oriented, it is most likely

in this case that the mounting between the sample and the rotational mount was not completely parallel, leading to an emergent relative tilt in the sample as the rotational mount was changed to measure along different axes. This leads to a changing asymmetry in the measurement of the band structure as a function of rotation. The change in tilt angle may also lead to a slight error in the calculated Fano-resonant wavelength if the tilt induces aberration in the optical field entering the spectrometer. However, extraction of the band parameters can proceed unimpeded in the vicinity of the gamma point, as the fitting algorithm is robust to slight changes, and overall errors in wavelength will be averaged out when the smoothing filter is applied to calculate the final two-dimensional band structure.

Most notably, there is a ~10nm shift in the resonance of the photonic bands between simulation and experiment. It is perhaps surprising that this appears to be the only main deviation as the measured metasurface was dramatically over-etched. Profile measurements show an etch depth of 223nm, which is 14nm over the intended partial etch depth of 209nm. Examining the simulated studies of partial etch errors and fill factor errors, we would anticipate this over-etching to drive the photonic band towards a parabolic dispersion, but the measured flat band dispersion indicates that an offsetting error in exposure most likely occurred in the lateral directions. While the fabricated chip had a sweep of parameters, the measured final device was the center device intended to be as close to the design parameters as possible, which ended up with offsetting errors that resulted in a similar dispersion to that which was designed.

The other main difference between simulation and experiment is a reduction in the contrast of the bands or equivalently in the amplitude of the Fano resonances. Returning to simulation and adding in an imaginary component to the refractive index shows that loss due to the silicon is the main contributor to this reduction in contrast of the bands. Design of photonic bands solidly in the infrared might avoid this issue, as the

absorption of silicon is lower, but would render it impossible to measure the photonic band structure with our current E-k spectroscopy setup, which is based on a CCD camera mainly sensitive in the visible wavelengths. However, with these two dimensional flat band designs verified, simpler measurements of narrowband filtering of an incident laser could be used to measure a device in the infrared regime.

The calculated two-dimensional band structure again agrees with simulation, although again note the 10nm shift in resonant wavelength. The symmetries and structure of the bands are the same although the experimentally measured dispersion for P-polarized light, while retaining a flat portion near the gamma point, does not have as flat of a dispersion farther out along the X axis. These two band structures characteristically agree, but it is worth noting that there is a somewhat of a fundamental problem in the two-dimensional band fitting in this case. Looking at the simulated and experimental band structures, there are clearly defined bands along the X and M axes, but at azimuthal angles of 15 and 30 degrees, there are two different bands present that split off of the flat band! In fact, the flat band is a mix of two different bands at every point in between the principal axes of the Brillouin zone. It is this structure that allows the bands to retain their necessary symmetries. If only a single band represented flat band resonance at the gamma point for both polarizations and that band remained flat out to the measured flat band numerical aperture, it would need to remain a single band even as the incident angle approached extremely oblique incidence. This is clearly not possible, as the structure does not have the necessary symmetries to support identical resonances in S and P polarizations at the X point in the Brillouin zone. It is maybe not revelatory that this "flat band" is actual two different bands, as simulation and measurement confirm that the dispersion is flat for both S and P polarizations. What may be surprising, however, is how the mixing between these two states occurs at different azimuthal angles.

9.2 Field Profiles

By examining the field profiles of the two-dimensional photonic flat bands we can begin to gain insight into the fundamental mode degeneracy behind this degenerate flat band phenomenon. Using rigorous coupled wave analysis (RCWA) to record the local field at the top surface of the device as a function of different incident angles and polarizations, we can see that the fields for S and P polarized flat band resonances along the X axis are localized in single sublattices depending on their polarization. For the measured device, this may seem expected and due to the elliptical symmetry breaking of the fundamental circular Lieb lattice, but it is a phenomenon reproduced in the circular Lieb lattice, as well. This sublattice localization is actually very characteristic of Lieb lattice flat bands.

While the field profiles may be simulated, it is much more difficult to experimentally measure near-fields in a metasurface with a subwavelength unit cell. However, recent work on measuring the near-field of a bound-state-in-the-continuum (BIC) metasurface via photoelectron microscopy is capable of resolving the field present in single meta-atoms [46]. This method could be used to experimentally measure the sublattice-specific field confinement that is shown in simulation. This separation of fields based on polarization and input angle also creates novel opportunities in tuning and emission control with flat band metasurfaces. By simulating the tuning of the refractive index in one of the sublattices, we can show a breaking of the degeneracy between the two polarized flat bands and separate one flat band into two. Conversely, if photoluminescent materials with similar indices but different emission profiles are deterministically placed within a given sublattice, there is a possibility of selective excitation to produce different outputs. This remains an interesting open area for further study.

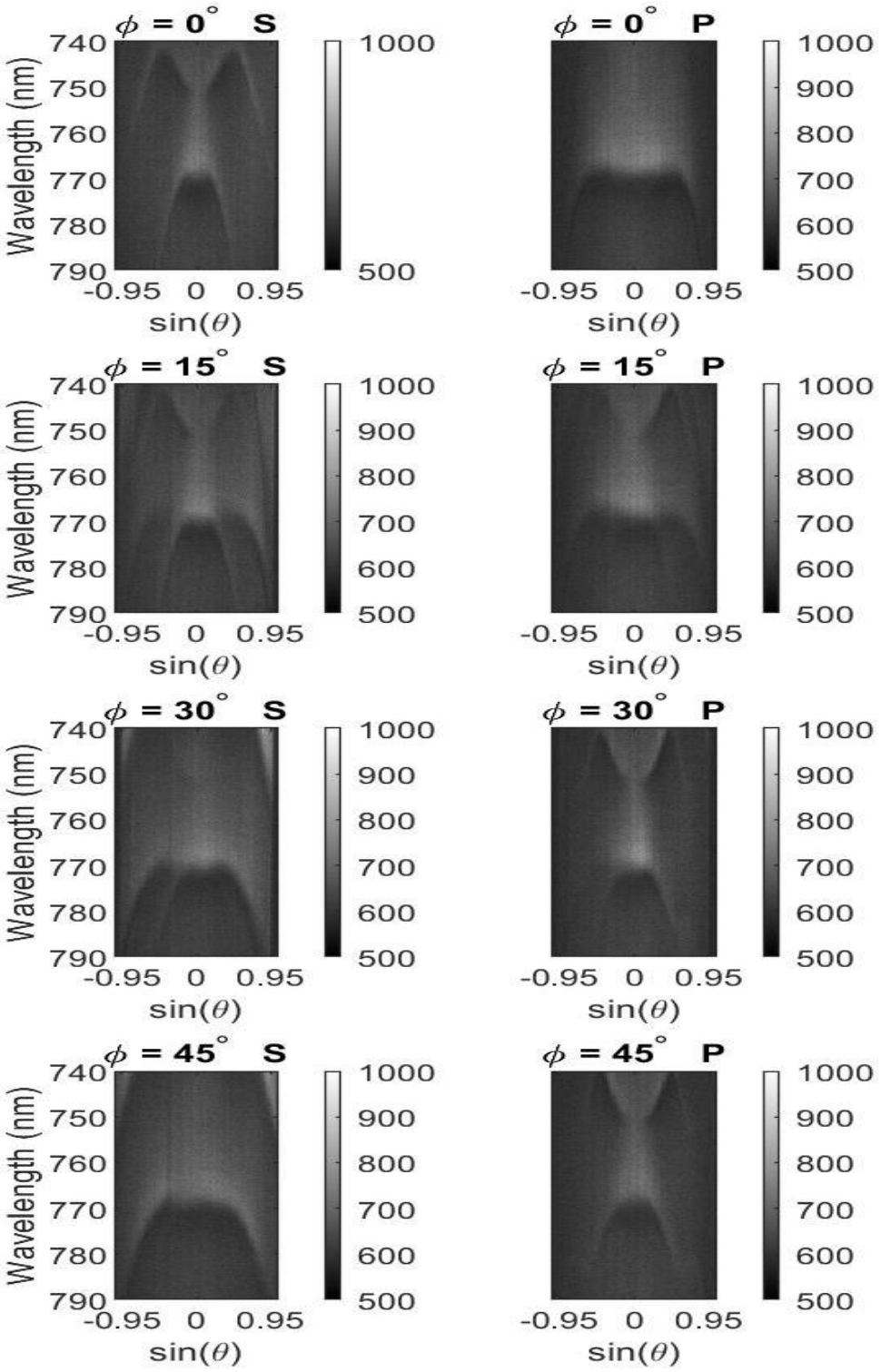

Figure 9.1: Experimentally measured band structure of the flat band metasurface along 15-degree rotational steps in azimuthal angle from along the X axis is in the Brillouin zone ($\phi = 0°$) to along the M axis ($\phi = 45°$) for both S and P polarizations.

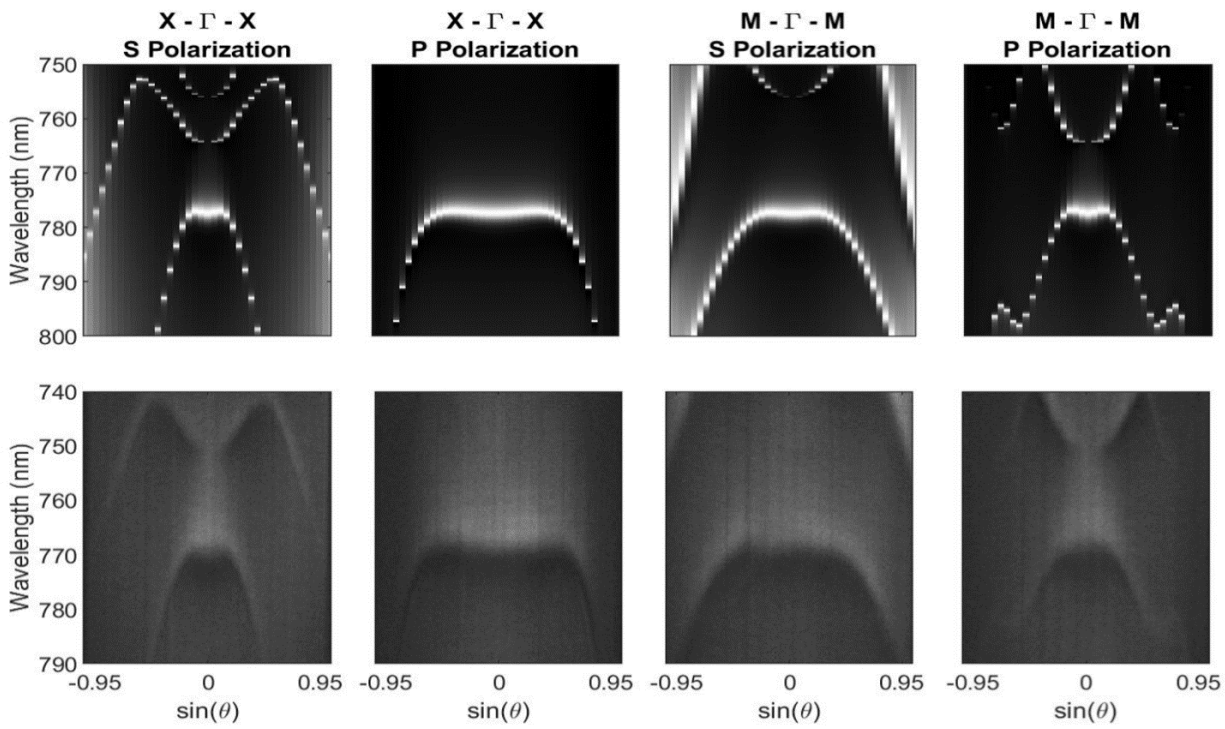

Figure 9.2: Comparison of simulated band structure with experimentally measured band structure for the Lieb lattice metasurface. Band structures up to the numerical aperture of the objective (.95) are shown along the X and M axes in the Brillouin zone for both S and P polarizations. Note a wavelength offset of 10nm between the simulation and experiment, which is most likely due to fabrication imperfections.

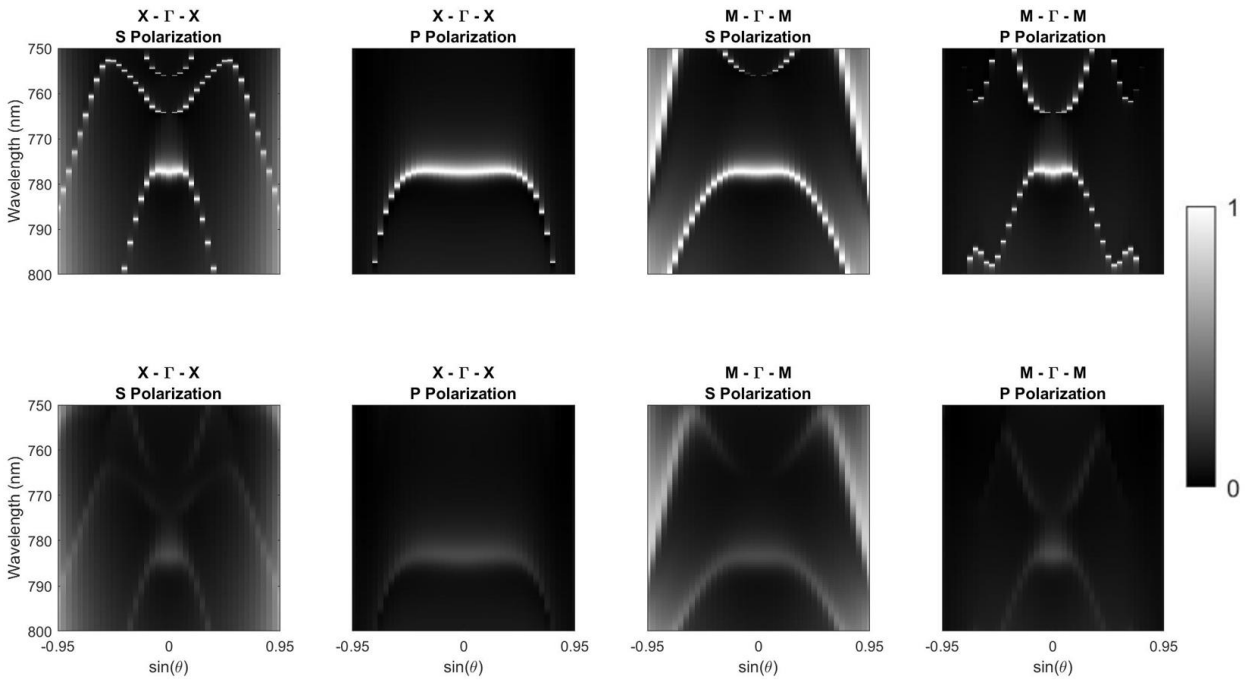

Figure 9.3: Comparison of simulated band structures with (bottom) and without (top) loss in the silicon. The top row of RCWA simulations assumes a defined refractive index of 3.67 for the silicon while the bottom row uses the Lumerical 'Silicon- Palik' material which includes an imaginary component of the refractive index. The color axis is identical between the two simulation results—note a significant decrease in the amplitude of the Fano resonance for the simulation including loss.

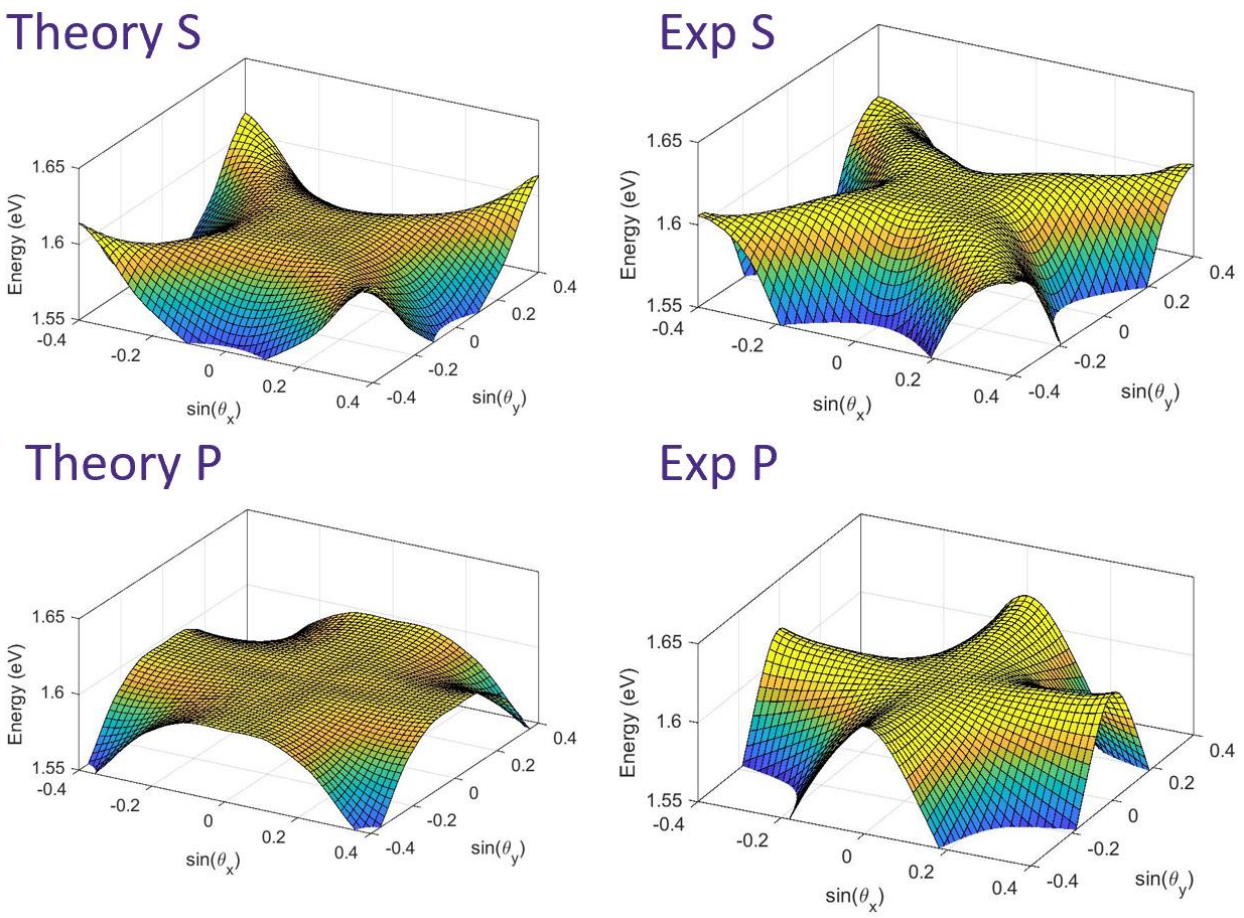

Figure 9.4: Extracted band structures shown for both S and P polarizations for the theoretically simulated and experimentally observed results.

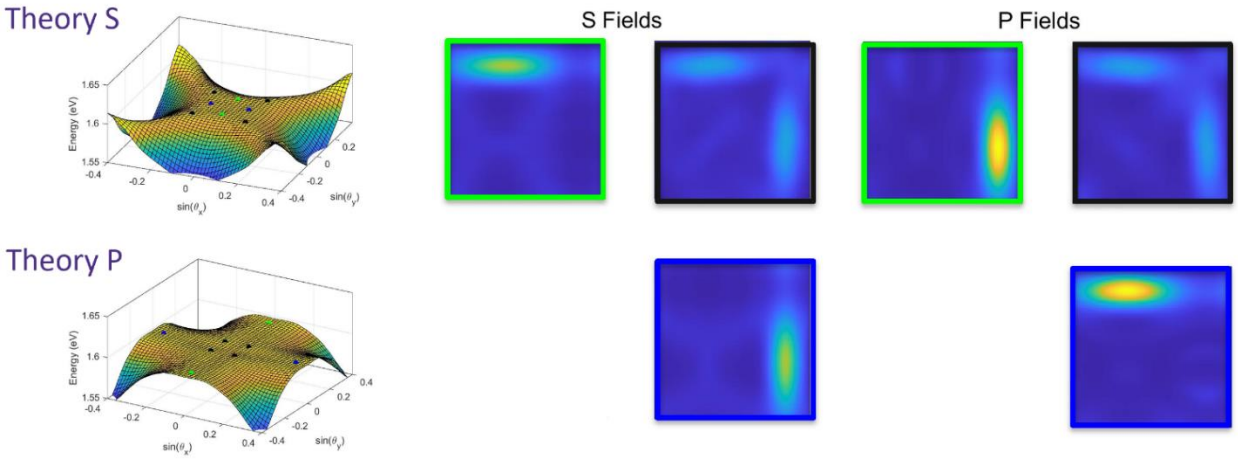

Figure 9.5: Limits of the flat band indicated on the two-dimensional band structure with corresponding unit cell field intensities shown. Note isolation of the field to the sublattices when excited along the principal axes of symmetry.

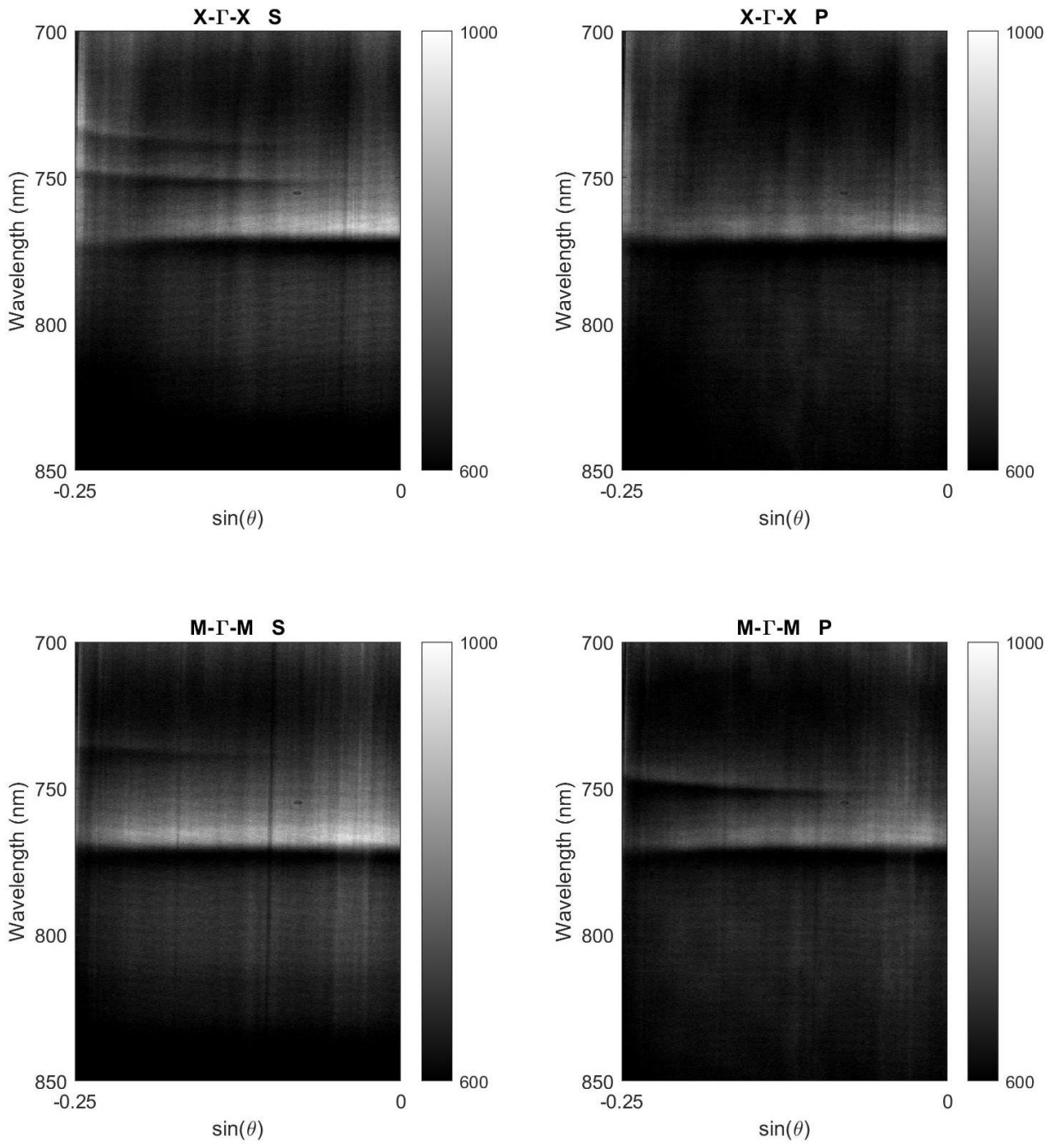

Figure 9.6: Reflection spectra of the flat band metasurface taken with a 10x objective up to a numerical aperture of .25. Note the extent of the flat bands out to ~8 degrees of half angle. Bound states in the continuum can also be observed with specific selection symmetries at ~730nm and ~750nm.

10. Applications

Photonic flat bands in metasurfaces can be viewed as a complex feat of symmetry engineering or simply as an angle-insensitive filter. Accordingly, there are both very theoretical and practical purposes for photonic flat band metasurfaces. While I enjoy pondering the more lofty and esoteric applications for flat bands, simple demonstrations are easiest with a new type of device, and I do believe that flat band devices could be quite useful for basic applications in the near future.

10.1 Angle-insensitive filtering

Angle-insensitive filtering is an important application where photonic flat bands are definitionally useful. Several existing approaches already exist, each with its own benefits and drawbacks. To begin with, a standard notch filter based on distributed Bragg reflectors (DBRs) has reasonable spectral discrimination but is not angle-independent or polarization independent. The fundamental reason behind the angle and polarization dependence of standard DBR-based filters is the inherent dispersion of the Fabry-Perot resonances creating their spectral filtering effect. It is thus entirely natural to attempt to create a dispersion-less resonance with which to filter light.

Using a collection of sub-wavelength particles or structures with well-defined resonances can result in isotropic filtering, as can easily be seen in fields as disparate as biology and astronomy when looking at organic coloring compounds or interstellar dust clouds. This most natural approach is certainly applied when filtering using absorptive dyes or other material, but artificial resonators of arbitrary wavelength have also been constructed. Most notably, metal and dielectric systems with patterned resonators have shown narrowband, angle-independent, and polarization independent absorption [47, 48]. This concept has even been integrated with phase-change-material to create tunable angle-insensitive resonances [49]. However, these metallic systems can have very high

absorption and narrowband operation in the mid to near infrared but are more difficult to implement in the visible regime.

With the angle-sensitivity in a standard DBR or Fabry-Perot notch filter coming from the dispersion of the optical cavity, the other clear approach is to compensate for this dispersion in the manner of achromatic lensing. That is, introduce a mirror or material with anomalous dispersion such that the dispersion of the cavity and the material cancel. This has been demonstrated with a variety of layered materials, mostly relying on plasmonic dispersion in the infrared range [50, 51]. Hyperbolic metamaterials with angle-insensitive filtering and tuning have also been shown by using graphene films [52]. Avoiding the use of lithography is extremely beneficial to the ease of fabrication for these structures, but often their resonances are quite broad.

Finally, metasurfaces coupled to guided-mode-resonators have previously been shown to form angle-independent filters. One-dimensional and two-dimensional metasurfaces coupled with guided modes have been designed to show greater angle-tolerance or polarization insensitivity in filtering, but do not rise to the level of engineering a flat band [53,54]. A combination of a grating and gradient index material has also been used to theoretically demonstrate angle-independent absorption in one dimension [55]. While designing an angle-insensitive filter is an important end goal, applying the framework of photonic band structure to this problem also allows for better description and analysis of the interplay between cavity resonances and incident angles.

10.2 Applications of Angle-Insensitive Filters

Angle-insensitive filters are an interesting technology in themselves, but their applications are manifold. Early pioneers in the field, investigating photonic crystals for dispersion compensation, foresaw the use of angle-insensitive filters in free-space optical communication, what might now be termed “lifi” [56]. Modern desire for hyperspectral

imaging also requires angle-insensitive filtering and display technologies are always looking to display the same image without regard for viewing angle [49]. The clearest application for angle-insensitive narrowband filtering might be in protecting imaging systems (whether human or machine) from unwanted laser beams. A pilot can reasonably anticipate that laser strikes on planes will overwhelmingly occur with green lasers, most likely at 532nm, and with this knowledge, an angle-insensitive 532nm laser filter could protect a pilot's vision while allowing for reasonably uncompromised broadband vision [57, 58]. Similarly, the threat of laser strikes on imaging satellites has substantially increased in the 2020s, and angle-insensitive laser filtering may help prevent dazzling lasers from disrupting imaging operations [59]. Just as optics spans many fields of interest, angle independent filtering is necessary at the largest and smallest scales imaginable.

A necessity in astronomical observation to remove certain spectral lines from all incoming angles to a telescope has led to the introduction of photonics in telescope systems and the application of the "photonic lantern" [60]. In this device, a multimode to single-mode mapping is accomplished to break out an entire field of view into many single mode fibers whereupon narrowband filters can be applied [61]. Astrophotonics is in its infancy and metasurfaces along with photonic band structure engineering may have a role to play in its future [62].

On the other side of physical scales, quantum computing with ions and neutral atoms has a need for angle-insensitive filters. Readout of a single trapped ion may depend on detection of a single photon, requiring a detector that presents a large solid angle to the ion. To this end, photodetectors have been integrated into the substrate of single ion traps for read out [63]. In order to prevent interference, a transparent conducting window made from indium tin oxide (ITO) is placed in between the ion and the photodetector. However, the photodetector will still detect all incoming light

whether from the trapped ion or from a background; integration of a narrowband filter that will function over a large solid angle is still required [64]. To this end, flat band metasurface filters or integrated flat band photodetectors could be used to integrate photodetection to ion traps and help enable scalable quantum computing.

10.3 Flat-Band Enhanced Photodetection

In many of these cases, angle-independent filters are paired with photodetectors, and to this end, I have assisted work in realizing a flat-band-based photodetector [65]. Previously, the combination of a Fabry-Perot resonator and a material for dispersion correction along with a photodetector had been used to show angle-insensitive narrowband photodetection [66]. In our work, we demonstrated a one-dimensional flat band photodetector that combined band structure engineering with absorption engineering in a crystalline silicon platform to show narrowband-selective photodetection over a range of incident angles. The photodetection responsivity was measured across different input wavelengths and showed a pronounced peak at the wavelength of resonance for the flat band photodetector. Additionally, measurements with a variety of input numerical aperture confirmed the flat band behavior of the photodetector. This one-dimensional photodetector was then rotated and optimized for two-dimensional flat band photodetection, albeit only at the center point of this "bullseye" photodetector. While this "bullseye" photodetector showed only marginal improvement in extension to two-dimensional photodetection, the two dimensional flat band design previously described could be integrated with a photodetector to demonstrate flat-band-enhanced photodetection. To demonstrate a small-footprint photodetector, the metasurface could be paired with a concentrating lens matching the numerical aperture of its flat band with an eye towards applications in free-space optical communications. Additionally, since a flat band can be engineered at any number of wavelengths, allowing for wavelength-selective photodetection, multiple photodetectors

could be stacked on top of one-another to sequentially absorb and detect longer and longer wavelengths of light. These stacks of selective photodetectors could even by patterned in an array for imaging. In this way a per-pixel hyperspectral imaging system could be designed, albeit with rather impractical fabrication requirements.

10.4 Integration of Phase-Change Materials

The orthogonal states enabled by certain flat bands open another potential avenue for the application of flat bands. Electro-optic modulation, such as with phase change materials can be used to tune the phase of transiting light without significant loss [67]. Advancements in integrating individually addressable phase change materials with single meta-atoms have been stymied by the distributed nature of modes in nonlocal guided-mode-resonator-based metasurfaces. However, in flat band metasurfaces, the existence of multiple modes at a single wavelength with clearly separated field distributions may allow for distinct control of each mode. In this way, flat band metasurfaces may increase the functionality of phase change materials, allowing for polarization and phase control in a combined system.

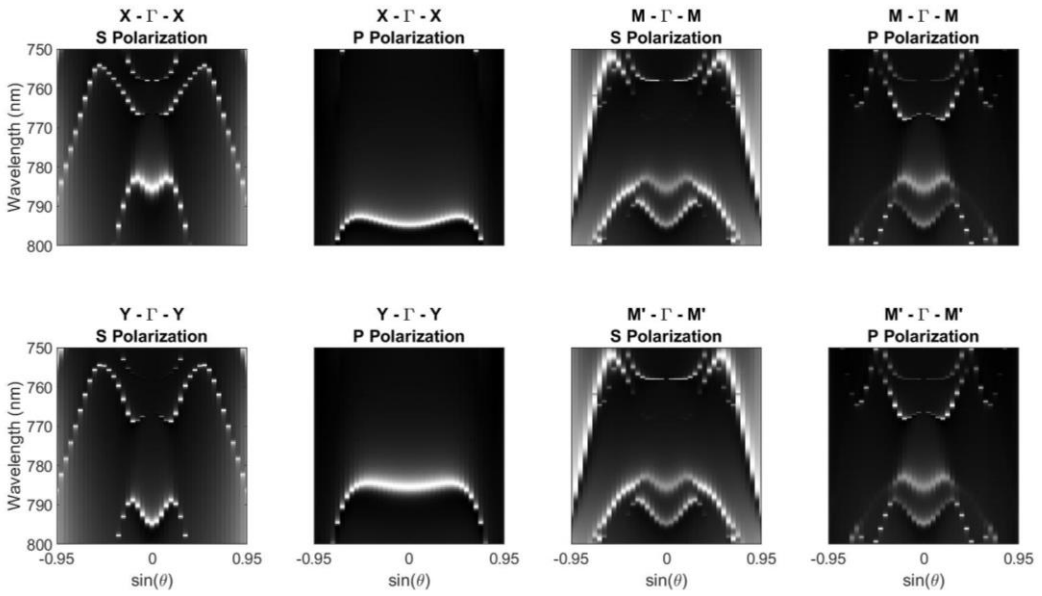

Figure 10.1: Simulated band structure of the 2-D flat band metasurface with a material having a refractive index of 1.5 added to one of the elliptical elements (for example, Poly(methyl methacrylate)). This breaks the degeneracy between the flat bands associated with field confinement in each of the elliptical elements (while also perturbing them out of a flat dispersion). This illustrates the ability of a refractive index change in only one of the elliptical elements to selectively shift bands of a specific polarization and incident angle. The band structure is now shown along the X, M, Y, and M' axes of the Brillouin zone with the M' axis at an azimuthal angle, $\phi = 135°$.

10.5 Emerging Applications

Ignoring both simple and impractical technological implications, there are more esoteric reasons to study flat band systems. Much recent attention has been paid to realizations of interesting Hamiltonians in photonic systems, such as pseudo-gravity potentials and pseudo-spin-dependent gauge fields [68,69]. Flat bands in photonic systems, due to their ability to host compact localized states, have been shown to host other exotic phenomena such as Aharonov-Bohm caging [70,71]. And interesting dynamics such as quantum scarring have been demonstrated in other systems and have been theorized to be present in flat band systems but have yet to be demonstrated in photonic metasurfaces [72-74]. With its potential for material integration, ease of

fabrication, and room temperature operation, a photonic metasurface system offers an attractive platform to study flat band dynamics.

11. Conclusion

To summarize, using sub-wavelength patterning, one-dimensional and two-dimensional flat band dispersion were experimentally demonstrated in dielectric metasurfaces. First, an existing design for realizing an infrared flat band response in silicon was transitioned to the visible regime by using a floating gallium phosphide membrane. This was then used to demonstrate dispersion engineering of visible emitters by measuring the photoluminescence of cadmium selenide nanoplatelets spin coated onto the device. The one-dimensional flat band design was then integrated into a photodetector by our lab to demonstrate angle-insensitive wavelength-selective flat-band-enhanced photodetection. I anticipate this specific usage to flat bands to have significant potential for various applications.

For the first time two-dimensional flat band dispersion was realized in an all-dielectric metasurface using sub-wavelength elements. Theoretical study of this design gives insight into tuning dispersion and band coupling of this two-dimensional flat band. Although the absorption coefficient of silicon at the flat band wavelength precludes its use as an effective angle-insensitive filter, this design can be adapted in the future to visible wavelengths and lossless materials. A thorough survey of possible applications in angle-insensitive filtering from astrophotonics to quantum computing and flat-band-enhanced photodetection was presented. The separation of modes by polarization and incidence angle was also noted, with a discussion of material integration for selective excitation or tuning. Future work may eventually allow for the realization of more esoteric applications.

It is my belief that we are only scratching the surface of the possible uses of dielectric metasurfaces. This new revolution in optics, enabled by sub-wavelength patterning, will have wide-reaching effects in many areas of technology and science.

Specifically, study of band engineering in metasurfaces continues and I hope that this work will help to inspire those previously unfamiliar with the field. Metasurfaces, and specifically the application of band structure engineering in dielectric metasurfaces, offers interesting theoretical challenges as well as potential applications across numerous fields.

References

Chapter 1: Introduction

[1] Joannopoulos, J. D., Villeneuve, P. R. & Fan, S. "Photonic crystals: putting a new twist on light". *Nature* 386, 143–149 (1997).

[2] Khorasaninejad, M. et al. "Metalenses at visible wavelengths: Diffraction-limited focusing and subwavelength resolution imaging". *Science* 352, 1190–1194 (2016).

[3] Munley, C. et al. "Inverse-Designed Meta-Optics with Spectral-Spatial Engineered Response to Mimic Color Perception". *Advanced Optical Materials* 10, 2200734 (2022).

[4] Audhkhasi, R., Fröch, J. E., Zhan, A., Colburn, S. & Majumdar, A. "Software-defined meta-optics". *Applied Physics Letters* 123, 150502 (2023).

Chapter 2: Background

[5] Sines, G. & Sakellarakis, Y. A. "Lenses in Antiquity". *American Journal of Archaeology* 91, 191–196 (1987).

[6] Kipp, L. et al. "Sharper images by focusing soft X-rays with photon sieves". *Nature* 414, 184–188 (2001).

[7] Neshev, D. N. & Miroshnichenko, A. E. "Enabling smart vision with metasurfaces". *Nature Photon.* 17, 26–35 (2023).

[8] Engelberg, J. & Levy, U. "The advantages of metalenses over diffractive lenses". *Nat Commun* 11, 1991 (2020).

[9] Banerji, S. et al. Imaging with flat optics: metalenses or diffractive lenses? *Optica* 6, 805–810 (2019).

[10] Overvig, A. C., Malek, S. C. & Yu, N. "Multifunctional Nonlocal Metasurfaces". *Phys. Rev. Lett*. 125, 017402 (2020).

[11] Overvig, A. & Alù, A. "Diffractive Nonlocal Metasurfaces". *Laser & Photonics Reviews* 16, 2100633 (2022).

[12] Malek, S. C., Overvig, A. C., Alù, A. & Yu, N. "Multifunctional resonant wavefront-shaping meta-optics based on multilayer and multi-perturbation nonlocal metasurfaces". *Light Sci Appl* 11, 246 (2022).

[13] Baba, T. "Slow light in photonic crystals". *Nature Photon.* 2, 465–473 (2008).

[14] Sakai, A. S. A., Hara, G. H. G. & Baba, T. B. T. "Propagation Characteristics of Ultrahigh-Δ Optical Waveguide on Silicon-on-Insulator Substrate". *Jpn. J. Appl. Phys*. 40, L383 (2001).

[15] Soljačić, M. et al. "Photonic-crystal slow-light enhancement of nonlinear phase sensitivity". *JOSA B* 19, 2052–2059 (2002).

[16] Mori, D. et al., "Experimental demonstration of wideband dispersion-compensated slow light by a chirped photonic crystal directional coupler," *Opt. Express* 15, 5264-5270 (2007)

[17] Xie, Y. et al. "Fractal-like photonic lattices and localized states arising from singular and nonsingular flatbands". *APL Photonics* 6, 116104 (2021).

[18] Hanafi, H., Menz, P. & Denz, C. "Localized States Emerging from Singular and Nonsingular Flat Bands in a Frustrated Fractal-Like Photonic Lattice". *Advanced Optical Materials* 10, 2102523 (2022).

[19] Leykam, D. & Flach, S. "Perspective: Photonic flatbands". *APL Photonics* 3, 070901 (2018).

[20] Mukherjee, S. et al. "Observation of a Localized Flat-Band State in a Photonic Lieb Lattice". *Phys. Rev. Lett*. 114, 245504 (2015).

[21] Xia, S. et al. "Photonic Realization of a Generic Type of Graphene Edge States Exhibiting Topological Flat Band". *Phys. Rev. Lett*. 131, 013804 (2023).

[22] Li, M. et al. "Fractal photonic anomalous Floquet topological insulators to generate multiple quantum chiral edge states". *Light Sci Appl* 12, 262 (2023).

[23] Baboux, F. et al. "Bosonic Condensation and Disorder-Induced Localization in a Flat Band". *Phys. Rev. Lett*. 116, 066402 (2016).

[24] Dang, N. H. M. et al. "Tailoring Dispersion of Room-Temperature Exciton-Polaritons with Perovskite-Based Subwavelength Metasurfaces." *Nano Lett*. 20, 2113–2119 (2020).

[25] Capitolis, J. et al. "Two-dimensional photonic metasurfaces for slow light-controlled photocatalysis". *Nano Select* 3, 108–117 (2022).

[26] Nguyen, D. X. et al. "Magic configurations in moiré superlattice of bilayer photonic crystals: Almost-perfect flatbands and unconventional localization." *Phys. Rev. Res*. 4, L032031 (2022).

[27] Nguyen, H. S. et al. “Symmetry Breaking in Photonic Crystals: On-Demand Dispersion from Flatband to Dirac Cones.” *Phys. Rev. Lett*. 120, 066102 (2018).

[28] Xu, Z., Kong, X., Chang, J., Sievenpiper, D. F. & Cui, T. J. “Topological Flat Bands in Self-Complementary Plasmonic Metasurfaces.” *Phys. Rev. Lett*. 129, 253001 (2022).

[29] Kajiwara, S., Urade, Y., Nakata, Y., Nakanishi, T. & Kitano, M. “Observation of a nonradiative flat band for spoof surface plasmons in a metallic Lieb lattice”. *Phys. Rev. B* 93, 075126 (2016).

[30] Xia, S. et al. “Demonstration of flat-band image transmission in optically induced Lieb photonic lattices.” *Opt. Lett.*, 41, 1435–1438 (2016).

[31] Harder, T. H. et al. “Kagome Flatbands for Coherent Exciton-Polariton Lasing.” *ACS Photonics* 8, 3193–3200 (2021).

[32] Zamir-Abramovich, K., Furman, N., Herrero-Parareda, A., Capolino, F. & Scheuer, J. “Low-threshold lasing with a stationary inflection point in a three-coupled-waveguide structure”. *Phys. Rev. A* 108, 063504 (2023).

[33] Yang, Y. et al. “Photonic flatband resonances for free-electron radiation”. *Nature* 613, 42–47 (2023).

[34] Inoue, T. et al. “General recipe to realize photonic-crystal surface-emitting lasers with 100-W-to-1-kW single-mode operation.” *Nat Commun* 13, 3262 (2022).

[35] Luan, H.-Y., Ouyang, Y.-H., Zhao, Z.-W., Mao, W.-Z. & Ma, R.-M. “Reconfigurable moiré nanolaser arrays with phase synchronization.” *Nature* 624, 282–288 (2023).

Chapter 3: Simulating Photonic Band Structure

[36] Moharam, M. G. & Gaylord, T. K. “Rigorous coupled-wave analysis of planar-grating diffraction”. *JOSA* 71, 811–818 (1981).

[37] Moharam, M. G., Grann, E. B., Pommet, D. A. & Gaylord, T. K. “Formulation for stable and efficient implementation of the rigorous coupled-wave analysis of binary gratings”. *JOSA A* 12, 1068–1076 (1995).

[38] Lalanne, P. & Morris, G. M. “Highly improved convergence of the coupled-wave method for TM polarization”. *JOSA A* 13, 779–784 (1996).

[39] Liu, V. & Fan, S. “S4 : A free electromagnetic solver for layered periodic structures.” *Computer Physics Communications* 183, 2233–2244 (2012).

Chapter 4: Energy Momentum Spectroscopy

[40] Dodson, C. M., Kurvits, J. A., Li, D. & Zia, R. “Wide-angle energy-momentum spectroscopy”. *Opt. Lett.,* 39, 3927–3930 (2014).

Chapter 5: Comparing Simulation and Experiment

[41] Miroshnichenko, A. E., Flach, S. & Kivshar, Y. S. “Fano resonances in nanoscale structures.” *Rev. Mod. Phys*. 82, 2257–2298 (2010).

Chapter 6: 1-D Flat Band Design

[42] Malek, S. C., Xu, Y. & Yu, N. “Resonant Metalenses Formulated from Quasi-Bound States in the Continuum for Visible Light”. in FW3D.8 (Optica Publishing Group, 2023).

Chapter 7: 1-D Flat Band Results

[43] Cho, W.; Kim, S.; Coropceanu, I.; Srivastava, V.; Diroll, B. T.; Hazarika, A.; Fedin, I.; Galli, G.; Schaller, R. D.; Talapin, D. V. "Direct Synthesis of Six-Monolayer (1.9 Nm) Thick Zinc-Blende CdSe Nanoplatelets Emitting at 585 Nm". *Chem. Mater*. 30, (2018)

Chapter 8: 2-D Flat Band Design

[44] Lieb, E. H. "Two theorems on the Hubbard model". *Phys. Rev. Lett*. 62, 1201–1204 (1989)

[45] Hamidi, M. et al. "Quasi-Babinet principle in dielectric resonators and Mie voids." *arxiv* (2023)

Chapter 9: 2-D Flat Band Results

[46] Boehm, A. et al. "Near-field Imaging of Optical Resonance Modes in Silicon Metasurfaces Using Photoelectron Microscopy". *arxiv*

Chapter 10: Applications

[47] Avrutsky, I. *et al.* "Angle- and polarization-independent mid-infrared narrowband optical filters using dense arrays of resonant cavities". *Opt. Express, OE* **27**, 37481–37493 (2019).

[48] Zhu, X., Fu, J., Ding, F., Jin, Y. & Wu, A. "Angle-insensitive narrowband optical absorption based on high-Q localized resonance". *Sci Rep* 8, 15240 (2018).

[49] Morden, D. et al. "Tunable angle-independent mid-infrared optical filters using GST-based micro resonator arrays". *Opt. Mater. Express* 12, 1043–1054 (2022).

[50] Chen, T.-A., Yub, M.-J., Lu, Y.-J. & Yen, T.-J. "Ultra-broadband, lithography-free, omnidirectional, and polarization-insensitive perfect absorber". *Sci Rep* 11, 5173 (2021).

[51] Sreekanth, K. V. et al. "A multiband perfect absorber based on hyperbolic metamaterials". *Sci Rep* 6, 26272 (2016).

[52] Kieliszczyk, M., Janaszek, B., Tyszka-Zawadzka, A. & Szczepański, P. "Tunable spectral and spatial filters for the mid-infrared based on hyperbolic metamaterials". *Appl. Opt.*, 57, 1182–1187 (2018).

[53] Wang, C.-M., Yu, C.-Y., Lin, S.-F. & Hsu, C.-L. "Angular-insensitive optical filtering based on meta-GMR". *Opt. Express*, 28, 18018–18026 (2020).

[54] Ng, R. C., Garcia, J. C., Greer, J. R. & Fountaine, K. T. "Polarization-Independent, Narrowband, Near-IR Spectral Filters via Guided Mode Resonances in Ultrathin a-Si Nanopillar Arrays". *ACS Photonics* 6, 265–271 (2019).

[55] Zheng, G., Cong, J., Xu, L. & Su, W. "Angle-insensitive and narrow band grating filter with a gradient-index layer". *Opt. Lett.*, 39, 5929–5932 (2014).

[56] Tetz, K., Chen, C.-H., Nakagawa, W., Wieder, H. H. & Fainman, Y. "Design, fabrication and characterization of narrowband angularly-insensitive resonant cavity filter". in *The 15th Annual Meeting of the IEEE Lasers and Electro-Optics Society vol. 2* 449–450 vol.2 (2002).

[57] Aerospace Medical Education Division, Federal Aviation Administration. "Laser Hazards in Navigable Airspace". (2021)

[58] Joshua Hadler, "Helping the Judicial System Understand Laser Strikes on Aircraft". NIST. (2014)

[59] Defense Intelligence Agency. “Challenges to Security in Space: Space Reliance in an Era of Competition and Expansion”. (2022)

[60] Birks, T. A., Gris-Sánchez, I., Yerolatsitis, S., Leon-Saval, S. G. & Thomson, R. R. “The photonic lantern”. *Adv. Opt. Photon*., 7, 107–167 (2015).

[61] Dinkelaker, A. N. et al. “Astrophotonics: introduction to the feature issue”. *Appl. Opt.*, 60, AP1–AP6 (2021).

[62] Jovanovic, N. et al. “2023 Astrophotonics Roadmap: pathways to realizing multi-functional integrated astrophotonic instruments”. *J. Phys. Photonics* 5, 042501 (2023).

[63] Reens, D. et al. “High-Fidelity Ion State Detection Using Trap-Integrated Avalanche Photodiodes”. *Phys. Rev. Lett*. 129, 100502 (2022).

[64] Brown, K. R., Chiaverini, J., Sage, J. M. & Häffner, H. “Materials challenges for trapped-ion quantum computers”. *Nat Rev Mater* 6, 892–905 (2021).

[65] Choi, Minho et al. “Nonlocal, Flat Band Meta-optics for Monolithic, High Efficiency, Compact Photodetectors”. *arxiv* (2023)

[66] Chen, C.-H., Tetz, K. & Fainman, Y. “Resonant-cavity-enhanced p-i-n photodiode with a broad quantum-efficiency spectrum by use of an anomalous-dispersion mirror.” *Appl. Opt*., 44, 6131–6140 (2005).

[67] Fang, Z. et al. “Non-volatile Phase-only Transmissive Spatial Light Modulators”. Preprint at https://doi.org/10.48550/arXiv.2307.12103 (2023).

[68] Nanjyo, K. et al. “Deflection of electromagnetic waves by pseudogravity in distorted photonic crystals”. *Phys. Rev. A* 108, 033522 (2023).

[69] Kiriushechkina, S. et al. “Spin-dependent properties of optical modes guided by adiabatic trapping potentials in photonic Dirac metasurfaces”. *Nat. Nanotechnol*. 18, 875–881 (2023).

[70] Mukherjee, S., Di Liberto, M., Öhberg, P., Thomson, R. R. & Goldman, N. “Experimental Observation of Aharonov-Bohm Cages in Photonic Lattices”. *Phys. Rev. Lett*. 121, 075502 (2018).

[71] Kremer, M. et al. “A square-root topological insulator with non-quantized indices realized with photonic Aharonov-Bohm cages”. *Nat Commun*. 11, 907 (2020).

[72] Zhang, P. et al. “Many-body Hilbert space scarring on a superconducting processor”. *Nat. Phys.* 19, 120–125 (2023).

[73] Kuno, Y., Mizoguchi, T. & Hatsugai, Y. “Flat band quantum scar”. *Phys. Rev. B* **102**, 241115 (2020).

[74] Kuno, Y., Mizoguchi, T. & Hatsugai, Y. “Multiple quantum scar states and emergent slow thermalization in a flat-band system”. *Phys. Rev. B* 104, 085130 (2021).